DEPARTMENT OF DEFENCE
DEFENCE SCIENCE & TECHNOLOGY ORGANISATION
DSTO

Prediction of Buffet Loads on Twin Vertical Tails Using a Vortex Method

Oleg Levinski

DSTO-RR-0217

Prediction of Buffet Loads on Twin Vertical Tails Using a Vortex Method

Oleg Levinski

Airframes and Engines Division
Aeronautical and Maritime Research Laboratory

DSTO-RR-0217

ABSTRACT

The work is concerned with the computation of F/A-18 vertical tail buffet due to LEX vortex burst using vortex methods of unsteady flow modelling. It is recognised that prediction of buffet loading requires accurate modelling of the unsteady pressure field past a burst LEX vortex. To reduce computational overheads associated with simulation of flow over the complete aircraft, a more generic delta-wing, twin vertical-tail configuration was used for initial studies. The aim is to generate an unsteady, vortex-breakdown flow using a delta wing and to place a vertical tail, which is cantilevered, downstream of the vortex breakdown flow. The paper describes the development of an unsteady vortex model for prediction of buffet loads and its validation against experimental data. Results of computation indicate that the vortex model is able to predict the onset of leading edge vortex breakdown and qualitatively describe the characteristics of unsteady buffet pressures arising on the rigid tail.

DEPARTMENT OF DEFENCE
DEFENCE SCIENCE & TECHNOLOGY ORGANISATION
DSTO

Published by

DSTO Aeronautical and Maritime Research Laboratory
506 Lorimer St
Fishermans Bend, Victoria 3207 Australia

Telephone: (03) 9626 7000
Fax: (03) 9626 7999

AR-011-966
July 2001

APPROVED FOR PUBLIC RELEASE

Prediction of Buffet Loads on Twin Vertical Tails Using a Vortex Method

Executive Summary

For the F/A-18 aircraft the ability to fly and manoeuvre at high angles of attack is achieved through a combination of the wing root leading edge extensions (LEXs) and twin vertical tails. The highly swept LEXs help to maintain lift during the post-stall flight regime by generating a pair of strong vortices which create additional 'vortex lift'. However, under certain flight conditions the initially stable vortices have a tendency to burst causing severe empennage buffeting and hence premature fatigue failures. Better understanding of the empennage buffeting problem is required for development of reliable fatigue usage monitoring systems and for the fleet management of the aircraft.

The work was initiated in an attempt to simulate the F/A-18 empennage buffet loading due to bursting LEX vortices and predict the vertical tail's dynamic response under various flight conditions. To allow for major characteristics of the tail buffet to be investigated without the computational overheads associated with modelling the flow over the complete aircraft, a more generic twin tail/delta wing configuration was used for these initial studies.

Although existing CFD codes can be applied for simulation of unsteady flows over delta wings, their computational requirements become prohibitive when it comes to more complex configurations. Therefore, a vortex approach was used for the development of an unsteady aerodynamics model that provided economy in computation by focusing the computational efforts in the areas of concentrated vorticity.

The paper describes the development and validation of the unsteady vortex model for the prediction of buffet loads on a vertical tail in inviscid incompressible flow. Results of flow simulations past a delta wing indicated that the vortex model is able to predict an onset of leading edge vortex breakdown and qualitatively describe its unsteady behaviour. Also, spatial and temporal characteristics of unsteady buffet pressures arising on the rigid tail were found to be in qualitative agreement with available experimental data.

Results indicate that the unsteady vortex method is able to predict vertical tail buffet loads and can be a useful tool for further study of buffet problems. Results of the work contribute to DSTO's existing body of knowledge on vortex breakdown and can assist in the International Follow On Structural Test Project (IFOSTP) of fatigue test on the F/A-18 aft fuselage and empennage.

Authors

Dr Oleg Levinski
Airframes and Engines Division

Oleg Levinski completed his Bachelor of Science in Aeronautical Engineering (Honours) at the Joukowski Institute of Aviation, Ukraine, in 1985. He has worked for several years with aircraft design and production organisations. He has been awarded 5 patents in the field of aeronautical/mechanical engineering and has published a number of papers. He completed his Doctorate at the University of Melbourne in 1997 and joined the Aeronautical and Maritime Research Laboratory the same year. He is currently a Research Scientist in the Airframes and Engines Division and his area of research is computational unsteady aerodynamics, structural dynamics and aeroelasticity.

Contents

Table of Figures

1. Introduction

During air-to-air engagements, military pilots of high performance aircraft often seek to manoeuvre at high angles of attack that allows for rapid turn rates often resulting in tactical advantages. For the F/A-18 aircraft this ability to fly and manoeuvre at high angles of attack is achieved through a combination of the wing root leading edge extensions (LEXs) and placement of the twin vertical tails.

At these high angles of attack, the airflow separates off the sharp leading edges of the highly swept LEXs and develops into a pair of strong vortices which pass over the wings and aft fuselage of the aircraft. The energetic LEX vortices help to maintain lift during post-stall flight by producing a favourable pressure field over the wings that creates an additional 'vortex lift'. The twin-tailed configuration of the F/A-18 is also designed to make use of these intense vortical flows in order to maintain directional stability of the aircraft at high angles of attack.

However, at some flight conditions, the vortices emanating from the highly swept LEXs have a tendency to burst producing highly turbulent swirling flow, which convects downstream and impinges upon the vertical tails. The LEX vortex breakdown prevents the development of the supplementary vortex lift and affects directional stability of the aircraft as the vertical tails get bathed in a highly disturbed breakdown flow. Moreover, the vortex bursting upstream of the empennage region produces unsteady load distributions on the tail surfaces causing severe buffeting and structural fatigue damage.

Considerable effort has been spent during the past decade in an attempt to understand and to predict the empennage buffet. It was revealed that onset of LEX vortex breakdown plays a major role in dictating the spectral content of the pressure fluctuations on the tail surfaces. Therefore, prediction of the empennage dynamic response during buffet should rely on accurate modelling the temporal and spatial characteristics of the unsteady pressure field past a burst LEX vortex. Despite some progress in our understanding of the phenomenon, the flow parameters that affect the breakdown and the physical processes governing its occurrence are still under investigation.

A significant reduction of the empennage buffet loads has been obtained as a result of fitting LEX fences to all the F/A-18 fleet aircraft. However, the use of the LEX fence has not resolved all the problems and the search for more effective solutions is still under way in order to further improve the service life of fleet aircraft and reduce their operational costs. Also, the design of future generation fighter aircraft is still focusing on high angle of attack manoeuvrability at high loading conditions, renewing the interest in the empennage buffeting problem.

2. LEX Vortex Breakdown

The complex fluid dynamics phenomenon known as 'vortex breakdown' or 'vortex core burst' can be encountered in a wide range of swirling flows. Peckham and Atkinson [1] were among the first investigators who encountered the phenomenon of vortex breakdown in their experimental study of flow past a highly swept delta wing at high angle of incidence. Since then, vortex breakdown has been the subject of intensive theoretical and experimental investigation. Despite all this effort, the causes of vortex breakdown are still poorly understood and its description is uncertain. The phenomenon still lacks a precise mathematical definition that would enable an accurate detection of its occurrence during numerical simulation. Therefore, an understanding of what vortex breakdown is and how it reveals itself, needs to be addressed.

2.1 Description of the Phenomenon

It was observed during experimental investigations in the flow over highly swept delta wings, that an increase in the angle of attack strengthens the leading edge vortices until eventually a sudden change occurs in the nature of the vortex cores. Initially a stable and well-defined vortex core is destroyed, or at least much diminished in strength and organisation. According to Benjamin [2], this abrupt and drastic change of vortex structure constitutes the leading edges vortex breakdown. Upstream of the breakdown location, the vortex core appears unaffected. Downstream of the breakdown, the flow is disorganised but sometimes can recover to the original state and can be followed by the appearance of another breakdown.

Ekaterinaris and Schiff [3] also describe vortex breakdown as a sudden change in the nature of the core, which they defined as a transition of the vortex core from jet-like to a wake-like flow. O'Neil, Barnett, and Louie [4] describe the breakdown effect as the rapid degeneration of a well-defined leading edge vortex into a substantially larger, more diffuse vortical flow region with relatively mild gradients. More precise definition of the vortex breakdown was suggested by Midkavi [5]. He defined the vortex breakdown as the flow structure that results when at some axial location on a vortex filament the axial derivatives are no longer small compared to the inverse of the vortex core size. Therefore, in the breakdown region the core size can be abruptly increased by an order of magnitude within a distance comparable to the core size.

Considerable insight into the essential features and nature of vortex breakdown has been gained during numerical and experimental investigation of the phenomenon at AMRL. Vortex breakdown in confined swirling flow has been studied computationally by Lopez [6] and Brown and Lopez [7]. The results of their simulations were found to be in excellent agreement with experiment. From their study of the distribution of physical quantities through the flow field it was suggested that the principal features of vortex breakdown in confined swirling flow can be described in terms of inviscid

phenomena alone. It was found that the initial divergence from the narrow core is the result of the upstream distribution of total head and angular momentum and subsequent waviness of the stream surfaces is caused by a stationary inertial or centrifugal wave. The development of multiple recirculation zones was found to be the result of generation of negative azimuthal vorticity through the stretching and tilting of vortex lines in this diverging inviscid flow.

Thompson [8,9] performed water tunnel studies of vortex flow over both simple delta wings and delta wings of more complex geometry. These studies revealed that the occurrence and axial position of vortex breakdown strongly depend on delta wing geometry and angle of incidence but are only weakly dependent on flow Reynolds number. He also investigated the flow over a $1/48^{th}$ scale model of the F/A-18 aircraft in the AMRL water tunnel [10] to study the effects of engine inlet flow rate, Reynolds number, position of control surfaces, *etc.*, on the axial position of LEX vortex burst.

Further experimental investigation included wind tunnel tests of the flow over the F/A-18 using a $1/9^{th}$ scale model, see Martin & Thompson [11] and Thompson [12]. Despite the substantial difference in Reynolds numbers, the results of water tunnel and wind tunnel tests showed reasonable agreement regarding the axial location of the LEX vortex breakdown. Also, the change in the axial position of the vortex breakdown with angle of attack had remarkably similar trends for all of the above tests.

The results of Lopez and Thompson, along with other experimental data from sub-scale and full-scale tests on flow over F/A-18 aircraft confirm that the principal features of LEX vortex breakdown are almost independent on Reynolds number. These findings suggest that the phenomenon of vortex breakdown is comprehensible in terms of an essentially inviscid, unsteady approach.

2.2 Numerical Investigation into Vortex Breakdown

Several attempts to compute the leading edge vortex breakdown that occurs over delta wings have been made using numerically intensive Euler and Navier-Stokes codes. For example, Hitzel [13] found that the Euler-methods are able to simulate leading-edge vortex breakdown despite neglecting viscous effects. He concluded that breakdown is almost independent of viscous effects and is presumably triggered by adverse pressure gradients, which decelerate the axial flow inside the vortex core. Thus, by the demands of continuity and the conservation of momentum the vortex core is forced to widen considerably, reducing the suction peaks and causing the nonlinear lift to decline.

Hitzel pointed out that his prediction of the leading edge vortex breakdown provided good agreement with experiments. However, he recognised that the solution exhibits very high total pressure losses in the vortex core, which he attributed to numerical errors introduced by the discretisation of the mesh. Furthermore, there were two other vortex-diminishing effects, which are intrinsic to most of the grid dependent methods.

One of these was the decreasing geometrical resolution of the vortex wake causing the vortices leaving the wing to flow into the coarser outer part of the computational domain. The other vortex diminishing effect was caused by the downstream boundary conditions. As stated by Hitzel, any boundary condition imposes some constant freeflow conditions and, therefore, the vortex must cease to exist at the boundary.

O'Neil *et al.* also investigated the flow over delta wings using Euler methods and repeated Hitzel's remarks that vortex breakdown is governed primarily by inviscid factors. In their numerical solution the breakdown effect was captured and a point of vortex breakdown was defined as the focus of maximum swirl angle, which falls in toward the vortex axis. O'Neil *et al.* concluded that occurrence of breakdown-like effects in the Euler solutions had definite trends, and was clearly not a result of arbitrary numerical coincidence. However, they too experienced the artificial dissipation, which is common to all Euler codes.

An attempt to simulate the vertical tail buffet in a delta-wing, twin vertical-tail configuration using Navier-Stokes code was undertaken by Kandil, Sheta and Massey [14]. They employed three sets of equations for the aerodynamic loads, the bending and torsional deflections and the grid displacements due to the twin tail deflections. As reported by the authors, many of the features of the experimental data of Washburn *et al.* [15] were captured by the computational model. Buffeting levels increased with the angle of attack and the case with the smallest spanwise separation between the tails produced the largest buffet loads, bending moments and deflections. Also, the frequencies of the tail loads and deflections decreased as the angle of attack increased, in agreement with experiment.

Although the Euler and Navier-Stokes codes can be successfully applied for the simulation of vertical tail buffet in delta-wing, twin-tail configurations, they require enormous computing resources to study more complex geometries. Thus, computation of time-accurate solutions of vortex breakdown in the flow over the complete F/A-18 aircraft using the above codes is at the very limit of the capabilities of modern supercomputers. Also, neither the Euler nor the Navier-Stokes codes can capture a sharp vorticity discontinuity without smearing it over a number of computational cells. Here, the mismatch between model-based prediction and actual behaviour is wholly attributable to numerical dissipation, which is inherent in the grid-dependent computational approaches.

An alternative to computationally intensive Euler and Navier-Stokes codes are the vortex-based methods which provide economy in computations by concentrating their efforts in the areas of high vorticity gradient. The vortex methods are particularly suitable for simulation of vorticity dominated regions, such as flow past a LEX. Besides the economy in computation, another advantage of vortex methods over grid-dependent Euler methods is in the way the initial vorticity is introduced. Usually, in Euler calculations the vorticity is already introduced at the start conditions. However, a proper way to evaluate the vorticity would be to simulate the real

time-dependent build-up of the flow starting from zero and evolving to the free-stream velocity. Within the vortex approach, this is accomplished by modelling the flow starting from rest and tracking a continuously developing vortex wake, which is not bound by a computational domain or grid. This eliminates the vortex diminishing effects and does not require an initial introduction of vorticity as found in Euler codes.

Despite the simplicity and robustness of the vortex methods, they have not received much attention as a tool for modelling vortex breakdown. One of the first attempts to simulate vortex burst in unbounded swirling flows by vortex method was undertaken by Nakamura, Leonard & Spalart [16]. Their vortex method seems to be well suited to the simulation of vortex breakdown, in that computational elements are simple straight filaments and are required only for the vorticity-containing regions where vortex breakdown is occurring.

The vortex filament method as used by Nakamura *et al.* does not explicitly include the effect of viscous diffusion and, therefore, does not account for the effect of Reynolds number on the mechanism of breakdown. However, as noted before, the process of breakdown itself is dominated by nonlinear inviscid vortex dynamics, which is well described by the unsteady vortex filament method. As argued by the authors, the primary role of Reynolds number is in shaping the internal structure of the vortex core upstream of the breakdown. Therefore, upstream velocity profiles within the vortex and the amount of swirling in the flow can be reproduced by simulation of vorticity convective and diffusive motions. In this way, the method can reflect changes in Reynolds number, and provide results comparable to those experimentally observed.

The results of the vortex simulations of Nakamura *et al.* are encouraging and show that the unsteady vortex filament method is able to capture the occurrence of vortex breakdown and provide a plausible solution for its unsteady behaviour. The vortex method successfully reproduced both axisymmetric and spiral types of breakdown and, according to the authors, can be used for simulation of other experimentally observed types of vortex breakdown.

Another attempt to determine if a vortex method can simulate vortex breakdown was undertaken by Lorey [17], who used an unsteady vortex lattice method in his computations of leading edge flow over a unit aspect ratio delta wing. The method was a hybrid of a vortex panelling method which described the lifting surface, and the vortex lattice method which was employed to model the development of unsteady vortex wake. The vortex model of Lorey produced a structure suggestive of vortex breakdown approximately at the two-thirds chord position. Despite this the occurrence of breakdown was not confirmed by the author, and he admitted that a more detailed investigation of the vortex wake would be required before making a final conclusion.

3. Vortex Methods for Unsteady Flow Modelling

Vortex methods simulate the unsteady fluid flows under the assumption of nonlinear dynamics of vorticity. Helmholtz [18] was the first who pointed out that vorticity in incompressible inviscid fluid is a material quantity and that it is carried by real fluid particles. So the real fluid flows at high Reynolds numbers can be simulated by regions of concentrated vorticity embedded in irrotational fluid. The vorticity-containing regions can be modelled by a combination of the vortex elements of appropriate strength or so-called discrete vortex lines, vortex rings or clouds of vorticity embedded in the flow which is potential in all other respects. The evolution of vortex elements can be tracked numerically in a Lagrangian or hybrid Euler-Lagrangian reference frame. As stated by the theorems of Helmholtz and Kelvin, the inviscid motion of vorticity in these regions is provided by the local fluid velocity, which in turn is determined kinematically from the vorticity field. As the area of application for the vortex model is limited mainly to incompressible flows, the Biot-Savart law of Green's functions can be applied to the calculation of the velocity field. As pointed out by Leonard [19], it is mathematically correct, and very convenient, to consider inviscid fluid dynamics in terms of concentrated vorticity regions, which induce motion on each other as an alternative to pressure-velocity considerations.

Helmholtz's ideas of inviscid vortex dynamics appeared extremely fruitful and led to the development of numerical methods which simulate fluid behaviour in a very natural way while obeying the known physical laws. As noted by Lewis [20], the vorticity method is rational in two senses. Firstly, in the empirical sense, the method simulates the actual physical processes taking place in fluid flow and secondly, it is rational in the sense that most of the known laws of fluid dynamics and mathematics are satisfied fundamentally. There are few numerical models which offer equal potential for such direct and economic simulation of nature and this is because the vortex is at the origin of all fluid flows.

Over the past decades, vortex methods have been developed and applied as a reliable predictive tool for a wide range of engineering problems. Their area of application has extended from simple inviscid potential flow calculations to the modelling of unsteady viscous flows by simulating the three-dimensional Navier-Stokes equations. The latter involves full treatment of boundary layer vorticity by simulating the process of its creation at the wall followed by its convection and viscous diffusion. Such computationally intensive vortex models are able to treat unsteady separated flows and can be used independently or in combination with inviscid vortex models in order to gain economies in computation. This ability of vortex methods to account for the complex features of fluid dynamics from within a single computational framework makes them a very attractive tool for a wide range of engineering problems.

Despite certain advantages of vortex methods, the significance of the traditional methods of computing unsteady fluid flows, such as Euler or Navier-Stokes codes should not be underestimated. These powerful yet computationally expensive methods are able to

provide very valuable information about the flow details. However, the limitation of the available computational resources calls for more economical methods, which can be used for preliminary investigations when it comes to such complex and computationally intensive problem as empennage buffet prediction.

3.1 Governing equations

Fluid flows are governed by the Navier-Stokes equations, which for incompressible viscous fluid flow may be expressed as

$$\frac{\partial \mathbf{u}}{\partial t} + (\mathbf{u} \cdot \nabla)\mathbf{u} = -\frac{\nabla p}{\rho} + \nu \nabla^2 \mathbf{u}, \tag{1}$$

$$\nabla \cdot \mathbf{u} = 0. \tag{2}$$

where $\mathbf{u}$ is a flow velocity,
p is a pressure,
ρ is the fluid density,
ν is a flow viscosity.

In homogeneous fluids, vorticity $\boldsymbol{\omega}$ is defined as

$$\boldsymbol{\omega} = \nabla \times \mathbf{u}. \tag{3}$$

Then in terms of vorticity, Equation (1) can be written as

$$\frac{\partial \boldsymbol{\omega}}{\partial t} + (\mathbf{u} \cdot \nabla)\boldsymbol{\omega} = \boldsymbol{\omega} \cdot \nabla \mathbf{u} + \nu \nabla^2 \boldsymbol{\omega}, \tag{4}$$

which represents the vorticity transport equation. This equation has a particular importance in vortex dynamics as it highlights the relationship between the velocity and vorticity in fluid flow. In this way, the pressure does not appear explicitly in the equation allowing anyone to find the velocity field without any knowledge of the pressure field.

The vorticity transport equation (4) represents simultaneous convection and diffusion of vorticity in the flow field. It also describes the concentration of vorticity due to vortex filament stretching, which is applicable only in three-dimensional flows. The solution can be obtained using the widely adopted fractional step method, which simulates the convection and the diffusion processes sequentially rather than simultaneously, see Leonard [19]. This can be achieved by solving Euler's equations by vortex method and using the proper numerical technique to model the diffusion equation. The required local velocities can be computed as the solution of Poisson's equation for the velocity field in terms of Biot-Savart integration. The result is a nonlinear system of ordinary differential equations giving the temporal evolution of vorticity coordinates. To complete the model, one should account for the process of vorticity production at the body surface to define the distribution of surface vorticity.

As one can see, there are three basic physical processes namely, the vorticity production, convection and diffusion, which have to be solved at each step of the computational procedure. Details of approaches adopted within the vortex method for simulation of these basic processes are discussed below.

3.1.1 Process of Vorticity Production

In a real flow, caused by the presence of viscosity, the well-known viscous boundary layer develops adjacent to the body surface. The essence of the majority of vortex methods is to replace this boundary layer by a region of concentrated vorticity, which causes a reduction of the fluid velocity from its local value to zero right on the body surface. For computational simplicity the real fluid flow can be represented as a bulk of irrotational inviscid outer flow separated from the actual body surface by the thin boundary shear layer, where the effects of viscosity and turbulence are simulated.

For high Reynolds number flows, the boundary layer will approach infinitesimal thickness. Thus, the body surface will be covered with an infinitely thin shear layer, which can be treated as a distributed vorticity sheet of strength $\gamma(s)$. Across this sheet the fluid velocity would change discontinuously from zero beneath the sheet on the body surface to V_S parallel to the surface just above the sheet. It can be shown that the rate of vorticity production in the shear layer is directly related to the pressure gradient, so vorticity creation is largely attributable to the dynamic behaviour of the outer flow.

According to Martensen [21], a statement of the Dirichlet boundary condition of 'no-slip' velocity at a point p on a body surface S can be expressed as

$$-\frac{1}{2}\gamma(p)-\frac{1}{4\pi}\int_S K(p,q)\gamma(q)\times dS_q + f(\tau_p, \mathbf{V}_\infty) = 0, \qquad (5)$$

which is a Fredholm integral equation of the second kind over the body surface where

- τ_p is a unit tangential vector to the body surface at point p,
- q is a variable point on a body surface S,
- K is a velocity singular kernel,
- f is a function of surface geometry and outer flow velocity.

The integral equation (5) describes the process of vorticity creation on the solid boundaries and can be used to define the distribution of vorticity over the body surface.

Another approach to the modelling of a solid boundary arises for the flow with infinite Reynolds number. In this case, the fluid is inviscid and the boundary shear layer can not be developed on the body surface. The fluid particles in contact with the body surface are no longer at rest and have some finite velocity. In this case the fluid velocity changes

discontinuously from zero value at the point which belongs to the body surface up to the value of V_S just above it. In this case, the body surface itself must be replaced by the vortex sheet of strength $\gamma(s)$. Here, the only appropriate boundary condition on the wall is the condition of zero normal velocity to ensure 'no-leak' velocity through the body surface. Such an approach is widely accepted in the potential inviscid flow calculation of the flow around slender bodies, see Belotserkovskii and Nisht [22].

Here, a statement of the Neumann boundary condition of 'no-leak' velocity at a point p on a body surface S may be expressed by the following integral equation

$$-\frac{1}{4\pi}\int_S K(p,q)\gamma(q)\,dS_q \times \mathbf{n}_p + f(n_p, \mathbf{V}_\infty) = 0, \tag{6}$$

where $\mathbf{n}_p$ is a unit normal vector at p. The physical interpretation of this equation is simply that the local vorticity density $\gamma(q)$ must be chosen such that, in the presence of an incident flow velocity $\mathbf{V}_\infty$, the resultant flow remains parallel to the body surface. It can be shown that imposing the integral equation (5) automatically satisfies the boundary condition of 'no-leak' velocity on a body surface provided there are no vortex or source distributions within the body profile.

3.1.2 Vorticity Convective Motion

Vortex methods as they are often used, deal with steady inviscid flow. In this particular case the local surface vorticity $\gamma(s)$ appears invariant with respect to time and is regarded as vorticity bound to the surface. However, it can be shown that even in the steady case the vortex sheet $\gamma(s)$, like an actual boundary layer which it represents, is continuously convecting downstream with a velocity equal to $\gamma(s)/2$. This principle applies to each local point S of the body surface, where the velocity varies from zero on the surface just beneath the vortex sheet to the $V_S = \gamma(s)$ just outside the sheet. Naturally, the local surface vorticity $\gamma(s)$ varies in magnitude along the wall that causes the different sheet convection velocities $V_c = \gamma(s)/2$.

The fact that the convecting vorticity is in a state of constant flux contains no contradiction with Kelvin's theorem of constancy of circulation. This is because vorticity is continually being created and destroyed at a body surface in an inviscid unsteady flow under the action of the surface pressure gradient imposed by the outer flow. As pointed out by Lewis [20], the surface vorticity numerical model is thus a direct simulation of the physical reality for an ideal inviscid or infinite Reynolds number flow, offering the most direct and natural boundary integral representation.

Following the adopted fractional step method, the vorticity diffusion part of the Navier-Stokes equations should be temporarily switched off when analysing the vorticity

convective motion. Therefore, vorticity convection along the body surface and in the wake must satisfy the inviscid vorticity transport equation

$$\frac{\partial \boldsymbol{\omega}}{\partial t} + (\mathbf{u} \cdot \nabla)\boldsymbol{\omega} - \boldsymbol{\omega} \cdot \nabla \mathbf{u} = 0. \tag{7}$$

The equations of motion of individual vortices are given by the value of the velocity field at their present locations

$$\frac{d\mathbf{x}_i}{dt} = \mathbf{u}(\mathbf{x}_i, t). \tag{8}$$

The spatial evolution of the flowfield can be obtained by integrating the above equation using the Adams-Bashford scheme, which is recommended for vortex methods [19]. However, in many cases, the first order Euler or forward differencing scheme can provide sufficient accuracy and computational efficiency compared to the higher-order schemes.

The required local velocities can be computed as the solution of Poisson's equation for the velocity field

$$\nabla^2 \mathbf{u} = -\nabla \times \boldsymbol{\omega}. \tag{9}$$

For a flow field without interior boundaries and with the fluid at rest at infinity, the solution to Poisson's equation (9) may be written as the Biot-Savart integral equation, which gives a velocity distribution induced by an area of concentrated vorticity, see Lamb [23]. Hence, one can get a nonlinear system of ordinary differential equations giving the temporal evolution of the vorticity field.

A natural consequence of the process of vorticity convection along the body surface is its shedding from certain separation points into the flow field. Although in a real flow the viscous boundary layer may separate spontaneously under various conditions, the assumption of a fully attached boundary layer is commonly used in inviscid potential flow calculations. In such an approach the flow is allowed to separate only at a finite number of prescribed separation points, such as the body trailing edge in order to satisfy the Kutta-Joukowski condition.

This is a quite reasonable approach if one is intending to stay with potential inviscid flow modelling. On the other hand it is possible to progress one step further with the above computational scheme, by attempting to simulate the behaviour of a real viscous boundary layer. In flows where boundary layer separation can occur, such as flow past bluff bodies, both processes of vorticity creation at the solid wall and subsequent transport of vorticity along the boundary needs to be simulated. Some vortex schemes rely on boundary-layer calculations, experimental information or other empirical knowledge to determine the location of separation points. However, a more natural approach is to create vortices at the boundary to maintain the 'no-slip' condition at the wall. The vortices thus created at the surface represent the developing boundary layer

and are allowed to move with the local flow velocity to satisfy the inviscid part of the vorticity transport equation (7). The diffusion of developing vorticity can be accounted for by allowing Gaussian vortex cores to increase, as suggested by Leonard [19] or by an alternative scheme of adding a random walk each time step, as introduced by Chorin [24]. If the mechanics of the boundary layer are being simulated correctly, vortices should separate quite naturally from the surface layer near the true separation points. Such a numerical scheme has been shown to converge to the solution of the Navier-Stokes equation as long as each sub-step is convergent, see Chorin [25].

3.1.3 Simulation of Vorticity Diffusion

Using the fractional step method again, convective motion should be temporarily switched off to analyse the vorticity diffusive motion. Therefore, to simulate the viscous diffusion part of the Navier-Stokes equation the following equation has to be solved

$$\frac{\partial \boldsymbol{\omega}}{\partial t} = \nu \nabla^2 \boldsymbol{\omega}. \tag{10}$$

There are several different numerical techniques that can be employed to simulate a process of vorticity diffusion. In the 'core spreading' technique, for example, the vorticity diffusion motion can be accounted for accurately by allowing the vortex core to increase, see [19]. Thus, the vortex core with vorticity distribution function ϕ_σ, similar to Gaussian distribution

$$\phi_\sigma(\mathbf{x}) = \frac{1}{\pi\sigma^2}\exp(-\frac{|\mathbf{x}|^2}{\sigma^2}), \tag{11}$$

and standard deviation σ can be used to satisfy the viscous part of the vorticity transport equation (4). To do so, it is required that σ^2 would grow linearly in time as

$$\frac{d\sigma^2}{dt} = 4\nu. \tag{12}$$

Another effective method, which approximates viscous diffusion in the statistical sense, was suggested by Chorin [24]. This method is based upon a numerical approximation of the diffused vorticity by an equivalent cloud of discretised vortex elements of similar finite structure. The original idea of the method is to subject all the free vortex elements to small random displacements, which produce a scatter equivalent to the diffusion of vorticity in the domain.

Chorin used the 'random walk' algorithm to study slightly viscous flow, and in his work on turbulence theory. As pointed out by Batchelor [26], much of the theory of turbulence is concerned with the behaviour of the spectrum of the flow at high frequencies. The

reason is that this behaviour seems to be independent of the particular flow under consideration. According to Chorin [24], the hope is that an understanding of this behaviour would suggest a way to incorporate these frequencies into a numerical method, because finite-difference methods in particular can handle only a bounded range of frequencies. The high-frequency range of the spectrum is associated with the less smooth part of the flow. The crucial assumption in Chorin's work is that the loss of smoothness in incompressible flow does not occur uniformly in each flow but is localised in certain regions, much in the same way as the high-frequency components of one-dimensional compressible flow are occasioned by the appearance of shocks. An argument was given to the effect that these rough regions consist of circular vortices. In order to match the observed spectra these vortices must have a core of universal structure. Their locations may be thought of as random. By constructing the flow from such elements, one ensures that the high-frequency range is taken into account.

To understand the essence of the random walk algorithm, let us examine the vorticity diffusion equation (10), which has a well-known solution of vorticity distribution in space and time

$$\omega(\mathbf{x},t) = \frac{\Gamma}{4\pi\nu t} e^{(-|\mathbf{x}|^2/4\nu t)}. \tag{13}$$

On the other hand, consider the following probability density function P of a Gaussian variable η with a zero mean and a standard deviation σ

$$P(\eta) = \frac{1}{2\pi\sigma^2} e^{(-|\eta|^2/2\sigma^2)}. \tag{14}$$

As one can observe the vorticity distribution in space and time defined by equation (13) agrees with the normal distribution curve of statistical theory if $\sigma = (2\nu t)^{1/2}$. Thus the solution of equation (10) can be achieved by spatial displacement of vorticity using a set of Gaussian random numbers, each having a zero mean and a standard deviation $\sigma = (2\nu t)^{1/2}$. This displacement due to vorticity diffusion can be added to the vorticity convective motion calculated from the solution of the convection problem.

As one can see, during the random walk algorithm the vorticity elements are treated as parcels of rotating fluid, which diffuse in much the same way as molecular diffusion. According to Lewis [20], it seems quite natural for a Lagrangian model of vortex dynamics, where fluid rotation is represented by an ensemble of small free fluid elements, that the motion should resemble particle motion and obey laws of diffusion similar to those observed at the molecular level.

Discussing the practical advantages of the random walk method, Chorin [24] pointed out the conflicting requirements of traditional grid methods for handling both the rapid vorticity rate change within a boundary layer and the grander scale of the subsequent downstream motion especially in high Reynolds number flows. Many important

applications such as unsteady wing motion involve complex problems of boundary layer stability and consequent vortex shedding. It is, therefore, of practical importance to develop a consistent flow model to simulate both of the above problems within a single computational framework. As noted by Chorin, in such a model the values of the velocity field near a boundary are not all computed but are merely sampled, with computational effort concentrated in regions of greatest interest.

Although the simulation of viscous diffusion of a point vortex by a random walk technique is quite straightforward, the problem of simulation of boundary layer vorticity diffusion presents a much more complicated task, especially at near-wall regions. According to Chorin [25], the aim in such regions need not be precise modelling at local eddy scale of resolution, but more a statistical sampling process using data obtained over a period of discrete time steps.

3.2 Discretisation of Vorticity Regions

According to the vortex method, the compact vorticity regions can be represented as a combination of parcels of vorticity having finite or infinitesimal cores. Several different approaches to the problem of spatial discretisation of vorticity-contained regions were developed aiming to improve the accuracy and computational efficiency of vortex methods.

3.2.1 Discrete Vortex Filaments

In many vortex-dominated flows the vorticity can be considered as confined to a finite number of isolated tubes of vorticity or vortex filaments. Similar to the point vortex representation in two-dimensional vortex flows, these flows in three-dimensional coordinates can be modelled by a system of space curves, each with zero cross-sectional area and constant circulation. For a single space curve C, the vorticity field then has the following representation

$$\boldsymbol{\omega}(\mathbf{x}) = \Gamma \int_C \delta[\mathbf{x} - \mathbf{r}(s)] \frac{\partial \mathbf{r}}{\partial s} ds, \tag{15}$$

where $\mathbf{r}(s)$ is a space curve of a vortex filament,
s is a parameter along the curve,
Γ is a vortex filament circulation ,
δ is the Dirac delta function.

According to the Biot-Savart law, the velocity field induced by this filament in an unbounded domain, with no interior boundaries, is given by

$$\mathbf{u}(\mathbf{x}) = -\frac{\Gamma}{4\pi}\int \frac{[\mathbf{x}-\mathbf{r}(s)]\times\dfrac{\partial \mathbf{r}}{\partial s}}{|\mathbf{x}-\mathbf{r}(s)|^3}\,ds, \tag{16}$$

where it is often convenient to represent the curvilinear vortex filament of arbitrary shape as a combination of rectilinear vortex filaments of constant strength.

Despite the vortex method faithfully solving the Euler equations, a system of discrete vortex elements may do a poor job of detailed representation of a physically interesting vorticity field. One of the first attempts to simulate a flow by a vortex method was undertaken by Rosenhead [27], who approximated the motion of a two-dimensional vortex sheet by tracking in time a system of point vortices. As a result, the non-smooth solutions were obtained in finite time for arbitrarily small initial disturbances. Later, numerous attempts of others to improve the solution of vortex sheet dynamics by using an increased number of vortices with more accurate time integration schemes did not resolve the convergence problem. In many cases the stability was lost and the vortices achieved a chaotic state of motion. This was caused by a strong singularity of Helmholtz vortices, which led to the infinitely high induced velocities near the vortex axis and/or critical velocity differences when interacting with the other vortices in close proximity. It resulted in computational instabilities, vortex system chaotic behaviour and physically impossible vortex layer self-intersection along and near the edges.

3.2.2 Vortex Filaments with Smoothed Kernels

Although the vortex elements with infinite core is the simplest method for vorticity discretisation and is suitable for a wide range of flow modelling problems, many investigators have used vortices with finite and corrected cores in their simulations. The idea of a smoothed singular kernel was widely used, as it yields more realistic vorticity distributions and bounded induced velocities for all the vortex elements. It was implicitly assumed, however that the use of such corrections does not affect the dynamics of large-scale structures of flow.

One of the earliest attempts to overcome the strong singularity of the point vortex were the two-dimensional vortex models of Rankine and Lamb [23], which introduced a correction to the vortex induced velocity field in different ways. For example, the velocity field of Rankine's vortex is defined as

$$v_\theta(r) = \frac{\Gamma}{2\pi r} \quad \text{for } r > r_c, \tag{17}$$

and

$$v_\theta(r) = \frac{\Gamma}{2\pi}\frac{r}{r_c^2} \quad \text{for } r < r_c, \tag{18}$$

with velocity gradient discontinuity at r_c. Thus, the flow in the inner area of Rankine's vortex rotates as a solid body, while remaining irrotational in the outer region. Therefore, all the vorticity is concentrated inside the small area of radius r_c, leaving the rest of the flow potential.

Lamb's vortex model has a vorticity distribution, similar to Gaussian distribution

$$\omega(r,t) = \frac{\Gamma}{4\pi\nu t}\exp(\frac{-r^2}{4\nu t}), \tag{19}$$

and velocity distribution as

$$v(r,t) = \frac{\Gamma}{2\pi r}[1-\exp(\frac{-r^2}{4\nu t})]. \tag{20}$$

Among the different vortex models only Lamb's model of an infinitely spreading vortex exactly satisfies the Navier-Stokes equations for an isolated viscous vortex in incompressible flow. However, as is well known, the exact solution can not be obtained for any system of such vortices because the Navier-Stokes equations are nonlinear and do not allow a principle of superposition of vorticity fields. Even a system of infinitely spreading Lamb's vortices will not satisfy these equations and only an approximate solution can be obtained.

3.2.3 Use of Cut-off Functions

Another attempt to overcome the strong singularity of a discrete vortex is the idea of using vortices with cores of constant and finite shape or vortex 'blobs', see for example Chorin [24] or Kuwahara & Takami [28]. In the vortex blob method, the vortex core is of axisymmetrical constant shape which is defined by a 'cut-off' radius and a 'cut-off' function to yield a description of vorticity distribution within the core. A blob can be described as a region of vorticity, which is convected in the fluid under the action of the other blobs. As vorticity in an incompressible inviscid flow is a material quantity that is carried by real fluid elements, then only the fluid particle locations have to be updated to simulate the evolution of the vorticity field. In a real fluid, the distribution of vorticity inside a blob would be distorted by the flow. In the vortex method, however, it is assumed that the blobs are translated as a whole.

The use of the vortex blobs allows smoothing of the singular kernel K, which connects velocity and vorticity for incompressible flows as follows

$$\mathbf{u}(\mathbf{x},t) = \int K(\mathbf{x}-\mathbf{x}')\,\boldsymbol{\omega}(\mathbf{x}',t)d\mathbf{x}'. \tag{21}$$

According to the vortex blob method, the velocity kernel K with a strong singularity is replaced by the smooth K_σ, a convolution of the velocity kernel K and a smoothing function f_σ as follows

$$K_\sigma = f_\sigma * K. \tag{22}$$

It is assumed that f_σ is defined as

$$f_\sigma(\mathbf{x}-\mathbf{x}') = \frac{1}{\sigma^n} f(\frac{|\mathbf{x}-\mathbf{x}'|}{\sigma}), \tag{23}$$

where n is the space dimension and $f(\mathbf{x})$ is a rapidly decreasing function which gives the vorticity distribution within the vortex element and which satisfies the normalisation requirement of

$$\int f(\mathbf{x})\, d\mathbf{x} = 1. \tag{24}$$

Here the shape or distribution function $f(\mathbf{x})$ is common to all vortex elements and is called the 'cut-off' function. The differences in the vorticity distribution between the vortices depend only on a parameter σ, which is a measure of the vortex spread and is referred as core size of the vortex filament. From the normalisation of $f(\mathbf{x})$, it can be noted that at a distance large compared with the core radius, the induced velocity may be calculated as if all the circulation was concentrated at the centre of the blob.

Thus, if the spatial configuration of the vortex filament with a blob-like core is defined by space curve $\mathbf{r}_i(s,t)$, then its vorticity field is given by

$$\boldsymbol{\omega}_i(\mathbf{x},t) = \Gamma_i \int f_\sigma[\mathbf{x}-\mathbf{r}_i(s,t)]\frac{\partial \mathbf{r}_i}{\partial s} ds. \tag{25}$$

Following Leonard [31], the velocity field induced by this filament can be determined as

$$\mathbf{u}_i(\mathbf{x},t) = -\frac{1}{4\pi}\Gamma_i \int \frac{[\mathbf{x}-\mathbf{r}_i(s,t)]\times\frac{\partial \mathbf{r}_i}{\partial s}\phi(|\mathbf{x}-\mathbf{r}_i(s,t)|/\sigma_i)}{|\mathbf{x}-\mathbf{r}_i(s,t)|^3} ds, \tag{26}$$

where smoothing function ϕ is determined by the choice of 'cut-off' function.

A number of core distribution functions have been employed to approximate the Navier Stokes equation in different ways. For example, Hald [30] introduced the

following class of cut-off functions, which enabled him to give the first convergence proof of a vortex method

$$f_\sigma = \frac{r^2}{\sigma^2}[14 - 105\frac{r^2}{\sigma^2} + 196\frac{r^3}{\sigma^3} - 140\frac{r^4}{\sigma^4} + 36\frac{r^5}{\sigma^5}], \qquad r < \sigma, \tag{27}$$

$$f_\sigma = 1, \qquad r > \sigma .$$

Results of Hald [30] and Leonard [31] have shown that in order to increase the spatial order of accuracy, one can use a core distribution function containing both signs of vorticity.

Later, Beale and Majda [32] designed vortex methods of arbitrary accuracy by choice of high-order explicit cut-off functions, such as

$$f_\sigma = 1 - e^{-r^2/\sigma^2}, \tag{28}$$

$$f_\sigma = 1 - 2e^{-r^2/\sigma^2} + e^{-r^2/2\sigma^2}, \tag{29}$$

$$f_\sigma = 1 - (\frac{r^2}{\sigma^2} - 1)e^{-r^2/\sigma^2}. \tag{30}$$

It was found by Beale and Majda, that the higher order methods yield a considerably more accurate representation of the velocity field than those of the lower order for moderate integration times. A comprehensive list of the most commonly used cut-off functions can be found in Chang [33].

The use of distributed vortex cores or vortex blobs yields more realistic vorticity distributions and bounded induced velocities for all the vortex elements. It can be shown that the vortex blob calculation scheme satisfies the principles of conservation of circulation, of impulse and momentum of impulse for the system of vortices with the same core sizes. However, it should be noted that the velocity field induced by a vortex of small but finite core is finite everywhere and is quantitatively correct far away from the vortex core. In close proximity to the vortex core the velocity field can be described only qualitatively, because the computational element carrying this vorticity is assumed to retain the same shape for all the time, though a real fluid element may suffer considerable strain, see Leonard [31].

Also, one should keep in mind that during the overlap of two or more vortices, the principle of Helmholtz, which states that for an inviscid fluid vorticity is a material quantity and is carried by real fluid elements, is no longer valid. Moreover, the principle of total energy conservation is violated as well and the amount of lost energy depends on the chosen core radius and is proportional to it.

Despite certain advantages of the high-order explicit cut-off functions, a simpler function of vorticity distribution within the core as proposed by Rosenhead [27] is adopted in the present study. The core radius is assumed to be time invariant and similar for all the vortex elements. Such scheme was found to be adequate for accurate representation of the velocity field modelled by well-spaced vortex filaments with low rate of adjacent cores overlapping.

3.3 Computational Algorithm

The general approach to the unsteady problem needs to be formulated and appropriate initial and boundary conditions introduced in order to derive a solution. Also, conditions of spatial and temporal discretisation of the body and its wake need to be determined. A numerical solution can be derived using the fractional step method, which provides a sequential simulation of the physical processes of vorticity development and evolution in the flow field, see Lewis [20].

To obtain a solution for the unsteady problem a numerical scheme is developed by the author where the vortex filament method is used to describe inviscid, potential flow aerodynamics. The method is a combination of a vortex panelling method, which describes the bound vorticity at the body surface, and an unsteady vortex lattice method, which is used to model the wake. A complete description of the unsteady vortex model is too extensive to be presented here and its details can be found in Levinski [34].

3.3.1 Formulation of the Unsteady Problem

Consider a lifting body S, undergoing an arbitrary motion in an infinite space of homogeneous incompressible fluid. In the general case the body motion can be described by its linear velocity $\mathbf{U}_0(t)$ and angular velocity $\Omega(t)$ with respect to some fixed inertial frame. Therefore, the resulting velocity of a point on a body surface S is given as

$$\mathbf{U}'(\mathbf{r}_S,t) = \mathbf{U}_0(t) + \boldsymbol{\Omega}(t) \times \mathbf{r}_S. \tag{31}$$

It is often convenient to analyse the unsteady flow problem in the coordinate system bound to the body such that absolute velocity field $\mathbf{W}(\mathbf{r},t)$ in the body-fixed reference frame can be defined as

$$\mathbf{W}(\mathbf{r},t) = \mathbf{V}(\mathbf{r},t) + \mathbf{U}(\mathbf{r},t), \tag{32}$$

where $\mathbf{V}(\mathbf{r},t)$ - is the velocity field, induced by the body and its wake,
$\mathbf{U}(\mathbf{r},t)$ - is the free-stream velocity.

Here, the unknown velocity field $\mathbf{V}(\mathbf{r},t)$ in the fluid domain must satisfy the Navier-Stokes equation

$$\frac{\partial \mathbf{V}(\mathbf{r},t)}{\partial t} + (\mathbf{V}(\mathbf{r},t)\cdot\nabla)\mathbf{V}(\mathbf{r},t) = -\frac{1}{\rho}\nabla p(\mathbf{r},t) + \nu\nabla^2\mathbf{V}(\mathbf{r},t), \tag{33}$$

as well as the continuity equation

$$\nabla\cdot\mathbf{V}(\mathbf{r},t) = 0. \tag{34}$$

It is known, that for high Reynolds number flows convective processes in the wake dominate, and the influence of viscous diffusion is minimal. For such flows with negligibly small viscosity, the assumption of fully inviscid flow can be justified and adopted. In this case, the original equation (33) in the inviscid fluid domain can be reduced to the Euler's equation for the unknown velocity field $\mathbf{V}(\mathbf{r},t)$

$$\frac{\partial \mathbf{V}(\mathbf{r},t)}{\partial t} + (\mathbf{V}(\mathbf{r},t)\cdot\nabla)\mathbf{V}(\mathbf{r},t) = -\frac{1}{\rho}\nabla p(\mathbf{r},t). \tag{35}$$

The induced velocity field $\mathbf{V}(\mathbf{r},t)$ can be assumed to be irrotational in the whole fluid domain except the body surface S and its trailing wake γ_p i.e.,

$$\nabla\times\mathbf{V}(\mathbf{r},t) = 0, \qquad \mathbf{r}\notin S\cup\gamma_p. \tag{36}$$

Then for the induced velocity field the velocity potential Φ exists such that

$$\mathbf{V}(\mathbf{r},t) = \nabla\Phi(\mathbf{r},t). \tag{37}$$

Therefore, according to Equations (34) and (37) the unknown induced velocity field can be found as a solution to the Laplace's equation

$$\Delta\Phi(\mathbf{r},t) = 0, \qquad \mathbf{r}\notin S\cup\gamma_p. \tag{38}$$

The fundamental objective of such a problem is to find the velocity potential $\Phi(\mathbf{r},t)$ that satisfies the Laplace's equation. It is known that under the above initial and boundary conditions, the problem has a unique solution, which gives us the unknown velocity potential $\Phi(\mathbf{r},t)$ in the fluid domain. As one can see, the assumption for the unknown velocity field $\mathbf{V}(\mathbf{r},t)$ to be potential considerably simplifies solution of the problem. However the decision to search for a solution of the Laplace's equation (38) instead of the original Euler's equation (35) implies an additional requirement that the basic vortex theorems of Kelvin and Helmholtz must be satisfied.

It is known from Lamb, that the solution for Laplace's equation can be obtained by a suitable choice of basic singularities such as doublets, sources or vortices. In fact, no one among these singularities has a special advantage over the others, as the potential flow can be modelled correctly by an appropriate distribution of either sources or vortices. This is guaranteed by the uniqueness theorems for Laplace's equation. But the numerical solution can be formulated at different levels of accuracy and computational efficiency. Therefore, it is particularly advantageous to consider the flow simulation method, based on vortex singularities, because such important physical processes as flow separation from the body surface as well as unsteady wake development and their interaction can be modelled using a single approach.

3.3.2 Initial and Boundary Conditions

As the process of flow development will be considered from the very beginning, it is reasonable to assume that during the period of time $t \le 0$ the fluid in the domain and the lifting body itself were in a state of rest. Then for $t > 0$ both the flow and the body are suddenly set in motion. According to vortex theory, the body unsteady motion will be accompanied by the development of its trailing wake which can be represented as a combination of vortex wake sheets γ_p. Therefore, the unknown velocity field $\mathbf{V}(\mathbf{r},t)$ in Equation (35) must satisfy the initial condition

$$\mathbf{V}(\mathbf{r},t) = 0, \quad \mathbf{U}(\mathbf{r},t) = 0, \quad t \le 0, \tag{39}$$

as well as the following boundary conditions:

1. For inviscid flow a statement of the Neumann boundary condition of 'no-leak' velocity at any point on a body surface S can be written as

$$\mathbf{V}(\mathbf{r}_S,t)\cdot\mathbf{n}(\mathbf{r}_S,t) + \mathbf{U}(\mathbf{r}_S,t)\cdot\mathbf{n}(\mathbf{r}_S,t) = 0, \tag{40}$$

   where $\mathbf{n}(\mathbf{r}_S,t)$ is a unit normal vector to the body surface at $\mathbf{r}_S$.

   Alternatively, for a slightly viscous flow, a statement of the Dirichlet boundary condition of 'no-slip' velocity at any point of the body surface can be imposed as

$$\mathbf{V}(\mathbf{r}_S,t)\cdot\boldsymbol{\tau}(\mathbf{r}_S,t) + \mathbf{U}(\mathbf{r}_S,t)\cdot\boldsymbol{\tau}(\mathbf{r}_S,t) = 0, \tag{41}$$

   where $\boldsymbol{\tau}(\mathbf{r}_S,t)$ is a unit tangent vector at the body surface at $\mathbf{r}_S$.

2. At infinite distance from the body and its wake the condition of induced velocities decay must be satisfied as

$$\lim_{r\to\infty} \mathbf{V}(\mathbf{r},t) = 0. \tag{42}$$

3. The Kutta-Joukowski condition of finite velocities must be satisfied at the lines p of trailing wake separation such that

$$\mathbf{W}(\mathbf{r}_p,t) \neq \infty. \tag{43}$$

As a consequence of the Kutta-Joukowski condition, a vortex wake will be created at the points of flow separation. The kinematic condition of normal velocity continuity

$$\mathbf{W}_i(\mathbf{r}_\gamma,t)\cdot\mathbf{n}_i(\mathbf{r}_\gamma,t) = \mathbf{W}_j(\mathbf{r}_\gamma,t)\cdot\mathbf{n}_j(\mathbf{r}_\gamma,t), \tag{44}$$

as well as pressure continuity

$$p_i(\mathbf{r}_\gamma,t) = p_j(\mathbf{r}_\gamma,t), \tag{45}$$

must be imposed on the upper i and lower j surfaces of the vortex wake sheet γ_P. This kinematic condition can be satisfied by allowing the trailing wake to move with the local fluid velocity while preserving its circulation, see Lamb [23].

3.3.3 Calculation of the Pressure Distribution

Having obtained the induced velocity potential $\Phi(\mathbf{r},t)$ from the solution of Equation (38), the unsteady velocity field $\mathbf{W}(\mathbf{r},t)$ can be determined. Then the unsteady pressure field can be calculated using the Cauchy-Lagrange equation [22] for inviscid incompressible flow as

$$P(\mathbf{r},t) = f(t) - \rho[\frac{\partial\Phi(\mathbf{r},t)}{\partial t} + \frac{\mathbf{W}^2(\mathbf{r},t)}{2}], \tag{46}$$

where the pressure function $f(t)$ can be determined from the boundary condition at infinity. Thus, if the induced velocities decay at infinite distance from the body and its wake, so that

$$\Phi(\mathbf{r},t) \to 0, \qquad |\nabla\Phi(\mathbf{r},t)| \to 0, \tag{47}$$

and assuming constant pressure at infinity, one can get

$$P(\mathbf{r},t) = P_\infty - \rho[\frac{\partial\Phi(\mathbf{r},t)}{\partial t} + \frac{\mathbf{W}^2(\mathbf{r},t)}{2}]. \tag{48}$$

Therefore, unsteady pressure coefficient on the body surface S can be defined as

$$C_p(\mathbf{r},t) = \frac{P(\mathbf{r},t)-P_\infty}{\rho\mathbf{U}_0^2/2} = 1 - w^2(\mathbf{r},t) - 2\frac{\partial\phi(\mathbf{r},t)}{\partial t}, \tag{48}$$

where $\mathbf{U}_0$ - is the flow field characteristic velocity,

$w = \mathrm{W}/\mathrm{U}_0$ - is a dimensionless flow velocity,

$\phi = \Phi/\mathrm{W}b$ - it a dimensionless velocity potential.

The unsteady pressure distribution can be found using the potential difference $\Delta\phi$ across the vorticity sheet γ (s), which is defined as

$$\Delta\phi(\mathbf{r}_S) = \phi_i(\mathbf{r}_S) - \phi_j(\mathbf{r}_S) = \Gamma_S, \tag{49}$$

where Γ_S is the circulation of a vortex element representing the vortex sheet at $\mathbf{r}_S$, and indices i and j refer to the upper and bottom sides of vorticity sheet γ (s), respectively.

Thus, the Equation (48) can be presented as

$$C_p(\mathbf{r}_S,t) = 1 - w^2(\mathbf{r}_S,t) - 2\frac{\partial[\phi(\mathbf{r}_S,t) - \phi(\mathbf{r}_K,t)]}{\partial t} - 2\frac{\partial\phi(\mathbf{r}_K,t)}{\partial t}, \tag{50}$$

where $\mathbf{r}_K$ is a coordinate vector of the leading edge stagnation point.

Then, according to the Equation (49)

$$\phi_i(\mathbf{r}_S,t) - \phi_i(\mathbf{r}_K,t) = [\phi_j(\mathbf{r}_S,t) + \Delta\phi(\mathbf{r}_S,t)] - [\phi_j(\mathbf{r}_K,t) + \Delta\phi(\mathbf{r}_K,t)]. \tag{51}$$

Assuming that $\Delta\phi(\mathbf{r}_S) = \Gamma_S$ and $\Delta\phi(\mathbf{r}_K) = \Gamma_K$, the above equation can be differentiated as

$$\frac{\partial}{\partial t}[\phi_i(\mathbf{r}_S,t) - \phi_i(\mathbf{r}_K,t)] = \frac{\partial}{\partial t}[\phi_j(\mathbf{r}_S,t) - \phi_j(\mathbf{r}_K,t)] + \frac{\partial}{\partial t}(\Gamma_S - \Gamma_K). \tag{52}$$

According to the boundary conditions, there is no motion allowed inside the body surface, so

$$\phi_j(\mathbf{r}_S,t) - \phi_j(\mathbf{r}_K,t) = 0, \tag{53}$$

and

$$\frac{\partial}{\partial t}[\phi_i(\mathbf{r}_S,t) - \phi_i(\mathbf{r}_K,t)] = \frac{\partial}{\partial t}(\Gamma_S - \Gamma_K). \tag{54}$$

Due to temporal discretisation of the problem, the above equation can be written as

$$\frac{\partial}{\partial t}[\phi_i(\mathbf{r}_S,t) - \phi_i(\mathbf{r}_K,t)] = \frac{(\Gamma_S^t - \Gamma_S^{t-1} - \Gamma_K^t + \Gamma_K^{t-1})}{\Delta t}. \tag{55}$$

By definition

$$\phi_i(\mathbf{r}_K, t) = \phi_\infty + \int_{+\infty}^{K} w_x dx, \tag{56}$$

where ϕ_∞ is the potential of free-stream velocity field and

$$\frac{\partial \phi_i(\mathbf{r}_K, t)}{\partial t} = \int_{+\infty}^{K} \frac{\partial w_x}{\partial t} dx. \tag{57}$$

Having defined all the unknown terms from the Equation (48), a distribution of unsteady pressure coefficient can be integrated over the whole body surface to obtain instantaneous values of aerodynamic forces and moments.

3.3.4 Separated Flow Modelling

Many flows past bluff bodies fall into the category of 'separated flows' when, under certain outer conditions, a boundary layer on the body surface becomes unstable and separates from the wall. The occurrence of boundary layer separation has a dramatic effect on lifting body aerodynamic characteristics. One of the main consequences is that the boundary layer separation brings the flow unsteadiness that complicates the study of such flows. The flow unsteadiness causes continuous change in boundary conditions on the body surface which are also affected by periodic wake return that involves a complex problem of boundary layer stability and secondary vorticity shedding.

For a typical range of Reynolds numbers the boundary layer dynamics is strongly influenced by both convective and diffusive activities taking place within the boundary layer which is further complicated by a strong influence of unsteady outer flow. Within the scope of vortex theory, a proper modelling of the unsteady separated flow past a bluff body must involve full treatment of boundary layer vorticity by simulating the process of its creation at the body surface followed by its convection and viscous diffusion. The corresponding numerical algorithm must account for the shedding of vorticity from the entire body surface and track the evolution of clouds of vorticity, which are free to convect and diffuse. The resulting model can be referred to as the full vortex cloud simulation of the Navier-Stokes equations.

An alternative to such a comprehensive though computationally intensive algorithm is the numerical scheme in which the boundary layer is allowed to separate only at a finite number of separation points, assuming potential flow modelling for the rest of the body. Here, the vorticity diffusion and convection activities within the body boundary layer are completely ignored, thereby substantially reducing the computational effort. It is implicitly assumed in this approach that the places of separation are known *a priori* and fixed at some particular places at the body surface. Such an approximation, as well as the assumption of fully attached flow on the rest of the body surface, is commonly used in

inviscid flow calculations. Following this simplified technique a surprisingly good prediction of overall aerodynamic characteristic may be obtained especially for sharp edged bluff bodies.

Some separated flows can be modelled in a combined way where on certain parts of the body surface the vorticity is allowed to shed only from prescribed separation points while on the rest of the body the natural separation is allowed. Otherwise, for a smooth surfaced body one may employ a viscous/inviscid numerical scheme, which uses traditional boundary-layer calculation at each step of the computational procedure to predict locations of vorticity shedding. However, to couple the solution with its viscous counterpart one needs to know the initial velocity of the shed vorticity as well as the trajectory of the separating shear layer leaving the body surface. This is because the resulting pressure distribution on a body surface is strongly dependent on the strength and position of all the shed vortices which are in close proximity to the body surface as well as clouds of vorticity in the near wake.

The well-known Kutta condition is usually applied to obtain a solution to the unsteady problem, but its use is justified mostly for steady flow cases. The use of the Kutta condition for unsteady flow modelling presents certain difficulties and the solution is usually based on some 'assumptions' and 'approximations'. As argued by many authors, because of the complications of the flow separation in the unsteady case, it is not obvious whether it should be resolved in the scope of a given numerical model, or considered separately using experimental results or some other considerations.

3.3.5 Representation of the Body and its Wake

Following vortex theory, a body surface and its wake can be replaced by infinitely thin layers of vorticity or vortex sheets consisting of spanwise and chordwise vortex lines of variable strength. Here, the presence of spanwise vorticity in a body vortex system is caused by a continuous change of the boundary condition at the wall brought about by the flow unsteadiness. The unsteadiness of the boundary conditions is also responsible for the presence of spanwise vorticity in a continuous vortex wake, separating from the body surface and its sharp edges. In the process of spatial discretisation of the continuous vorticity layer, the curvilinear vortex lines of variable intensity can be represented as a system of rectilinear chordwise and spanwise vortex filaments of constant strengths.

An extension of this model to the more general case of a viscous separated flow encounters certain difficulties. The presence of viscosity requires the vorticity diffusion to be included in the algorithm, which presents a problem for the integrity of the vortex wake sheets. The viscous diffusion of the isolated vortex filament can be simulated in a quite natural way using, for example, the random walk method, but the solution is not so straightforward for a system of vortex filaments, representing a vorticity sheet. Helmholtz's vortex theorem requires the vortex sheet to be self-conserved at all times, prohibiting random displacements of the vortex filaments.

One of the ways to overcome this difficulty is to build the vortex sheet from closed vortex elements, such as vortex panels or vortex rings. In this way each of the vortex elements will be free to undergo random displacements due to viscous diffusion and subsequent convective motion, without violating the principle of vorticity conservation. In some respects, such a numerical scheme will be similar to the 'vortex particles' algorithm, although having an advantage of better spatial representation of the vorticity field.

3.3.6 Temporal and Spatial Discretisation Scales

An algorithm for simulation of separated flow past a bluff body usually employs an iterative time marching scheme in which one system of vortex elements is shed from the body surface at every time step. It can be shown that the accuracy of such a model depends on a correct balance between the scales of spatial and temporal discretisation of the unsteady problem. Here, selection of an appropriate time step of the computational procedure should be based on average displacements of vorticity due to its convective and diffusive motions.

For high Reynolds number flows with dominating influence of convection over diffusion, an appropriate spatial discretisation of the body must correspond to the scale of vorticity convective motion. According to vorticity inviscid dynamics, an average convective displacement Δl_c of the vorticity in a shear layer can be defined as

$$\Delta l_c = \frac{1}{2} U_0 \Delta t_c, \tag{58}$$

where U_0 is a free-stream velocity and Δt_c is time step based on vorticity convective motion. A link between the convection displacement of vorticity Δl_c governed by inviscid vorticity dynamics and the corresponding scale Δs of the body surface discretisation may be defined as

$$k = \frac{\Delta l_c}{\Delta s}, \tag{59}$$

where k is in the range of [0...1].

Also, it can be shown that the average diffusive displacement Δl_d of the vortex element obtained from the vorticity diffusion equation (13) can be approximated as

$$\Delta l_d = (4\nu \, \Delta t_d \ln 2)^{1/2}, \tag{60}$$

where Δt_d is time step based on the diffusive displacement of vorticity.

A reasonable approach would be to maintain equal scales of vorticity motion due to convection and diffusion and that can be achieved by equalising Δl_c and Δl_d leading to

$$\Delta t_c = \frac{\Delta t_d \nu \ln 2}{U_0 k \Delta s}. \tag{61}$$

Introducing the number of vortex elements $M = l/\Delta s$ approximating the body surface and Reynolds number $\mathrm{Re}_l = U_0 l/\nu$, the above equation may be expressed as

$$\Delta t_c = \frac{\Delta t_d M \ln 2}{\mathrm{Re}_l k}, \tag{62}$$

where l is the body characteristic length.

However, it can be noticed from the above relationship that enforcing equal temporal discretisation scales Δt_c and Δt_d for convection and diffusion will lead to computational difficulties at high Reynolds number flows as the number of vortex elements required to approximate the body surface is $O(\mathrm{Re})$. Moreover, the related time increment becomes excessively small imposing severe pressure on computational requirements and making a computation of typical unsteady flows impractical.

To avoid computational difficulties during simulation of high Reynolds number flows, one can select different Δt_c and Δt_d time steps as, according to the fractional step method, solution to Equation (4) can be obtained using different time increments for its convective and diffusive parts, see Lewis [35]. A substantial economy in computation can be achieved using this approach, as only one random walk for simulation of vorticity diffusion needs to be performed after completion of several convection steps. However, the same average displacement of the vorticity due to its convective and diffusive motions will still be maintained.

4. Computation of Vertical Tail Buffet

Although an ultimate aim of the work is to predict unsteady buffet pressures on the F/A-18 empennage surfaces, a more generic geometry can be used for initial studies. It can be shown that the vertical tail buffet problem can be simulated efficiently using a simple delta-wing, twin vertical-tail configuration. The idea is to generate an unsteady, vortex-breakdown flow using a delta wing and to place a vertical tail, which is cantilevered, downstream of the vortex breakdown flow. The wing aspect ratio, angle of attack and flow conditions have to be carefully selected in order to produce unsteady breakdown of the leading-edge vortex cores. Then a computational model

should be able to demonstrate the development of the tail buffet due to the unsteady loads produced by the vortex breakdown flow.

The delta-wing, twin-tail configuration is well suited for the task because it contains all the pertinent physics involved in the development and burst of a leading-edge vortex and its subsequent interaction with the vertical tails. In this way, the buffet problem is isolated from the whole configuration and the computational resources are focused on a small region for higher resolution. It allows for major characteristics of the vertical tail buffet to be investigated without computational overheads associated with simulation of the flow over such complex configurations as a complete F/A-18 aircraft.

4.1 Past Experimental and Numerical Studies

An extensive wind-tunnel investigation of the delta-wing, twin-tail configuration has been conducted by Washrurn *et al.* [15] in order to examine the mechanisms of vortex-tail interactions. The leading edge vortices were generated by a sharp-edged 76 degree delta wing with twin vertical tails mounted aft of the wing. The model included both a dynamically scaled flexible tail and a pressure instrumented rigid tail so that mean and unsteady flexible tail response and unsteady tail surface pressure measurements on the rigid tail were obtained. The investigation included a parametric study of the effect of chordwise and spanwise tail location on the buffeting characteristics of vertical tails. The experimental results showed that the aerodynamic loads are more sensitive to chordwise tail location than its spanwise location. It was also shown that the buffeting response and excitation were reduced as the tails were moved laterally towards the vortex core. Although the tail location did not affect the upstream trajectory of the delta wing vortex, it affected the location of vortex core breakdown. The tail location also affected the global structure of the flowfield and the aerodynamic loads arising on a buffeted tail.

Past numerical studies of the delta-wing, twin-tail configuration were performed by Kandil *et al.* [14] using a set of unsteady, compressible, full Navier-Stokes equations and a set of coupled aeroelastic equations. The model consisted of F/A-18 twin tails, which were cantilevered at the trailing edge extension of the 76-degree delta wing. A solution was obtained for the uncoupled bending and torsional tail response due to unsteady loads produced by the leading edge vortex burst. The configuration was investigated for two spanwise separation distances, namely the midspan location with 56% spanwise separation distance, and the inboard location with 33% spanwise separation distance between the tails. However, the results were limited to an angle of attack of 32 degrees only. Results of numerical simulations showed that for the midspan location of the tails, the vortex breakdown flow was located inside the region between the twin tails. For the inboard location case, the area of vortex breakdown was split by the tails into an inner vortical flow between the twin tails and outer vortical flow outside the vertical tail. It was observed that in both cases, the location of vortex breakdown moved forward due to the twin tail dynamic response.

Although, the numerical results of Kandil *et al.* are in qualitative agreement with the experimental data of Washrurn *et al.*, the predicted magnitude of the deflections for the midspan location case is larger than that of the inboard location case. This is the opposite to that experimentally observed but can be explained by geometrical differences between the above two configurations and the limiting of the numerical solution to the uncoupled bending-torsion case only.

4.2 Computational Model Description

In the present study, a delta-wing, twin vertical-tail configuration similar to that of Kandil *et al.* is used to computationally simulate the vertical tail buffet problem. The computational model consists of a sharp-edged, 76-degree leading edge sweep delta wing (aspect ratio of one) and swept-back F/A-18 twin tails, see Figure 1. Both the delta wing and twin tails are of zero thickness. Each of the tails is of aspect ratio 1.2. The chord length at the root of the tail is 0.4 and at the tip is 0.159. Each tail has a sweepback angle of 35 degrees for a spanwise line at their quarter chord. The tails are cantilevered on the upper surface of a trailing edge extension of the delta wing. The tip of each tail is inclined outboard such that dihedral angle between the two tails is 40 degrees. Each tail is installed at 1 degree of incidence to the plane of symmetry by moving its trailing edge inboard. The spanwise separation distance between the tails is 50% of the delta wing span.

A total of 2986 closed vortex rings, or panels are used for spatial discretisation of the computational model, see Figure 2. A unit aspect ratio delta wing is modelled using 33 rows and 66 columns of vortex elements, forming the 2178 quadrilateral panels. The vortex system of the trailing edge extension continues the discretisation pattern of the delta wing and is represented by 416 rectangular panels while each of the vertical tails is modelled by 14 rows and 14 columns of trapezoidal panels. The vertex of each quadrilateral element represents a node.

On the wing and tail surfaces, the no-penetration condition is enforced. The unsteady wake is modelled as a vortex sheet, composed of vortex panels, which emanates from the sharp edges of delta wing, trailing edge extension and vertical tails. Computational simulation of the flow over the delta-wing, twin-tail configuration is accomplished under the assumption of symmetrical flow so only half of the model and its wake is considered in the analysis.

4.3 Results and Discussion

A number of sub-scale and full-scale experiments [10,11,35] on F/A-18 tail buffet provided valuable information about buffet pressure distributions, dynamic response of the vertical tails and some details of the flowfield in the vertical tail region. In order

to build upon the database generated by the experiments, the results of the numerical predictions are analysed in a manner similar to the experimental test data. However, a few problems with the interpretation of experimental and numerical results were identified in the past. Here, analysis of the experimental results indicated that the spatial resolution of the buffet pressure measurements has a pronounced effect on the integrated values such as vertical tail normal force and bending moment, see James & Meyn [37]. During computation the higher grid density on the tail surface, compared to the sensor densities in the experiments, helps to provide more detailed information about the flowfield over the tail surface. However, an attempt to analyse the computational data using only those surface pressure values obtained in locations used in the full-scale experiments did not improve the comparison. As reported in [37], the differences between the several integration methods were not as large as seen in the experimental data and the cause of the discrepancy was not identified. Thus, it should be noted that the limited number of pressure transducers used in the tests affects the validity of comparison with numerical predictions as some important information about the measured pressure distribution appeared to be lost.

Another issue that affects a proper comparison between experimental data and results of predictions is the length of computed and experimental time histories of unsteady buffet pressures. The computed time histories typically have relatively short sample times, compared to the experimental results, because of the substantial computational resources required for each second of real-time data. The short sample times can limit the usefulness of numerical predictions in resolving time-dependent data such as unsteady buffet pressures where statistical averaging of time histories is necessary. The computationally inexpensive vortex model can improve upon the previous CFD computation by increasing the amount of real time data computed, but the length of the computed time histories and level of resolution are still limited by the computer resources available.

4.3.1 Development and Breakdown of Leading Edge Vortex

Experimental investigation of the vertical tail buffet of the F/A-18 models in sub-scale and full-scale wind-tunnel tests indicated that the LEX vortex breaks down ahead of the vertical tails at angles of attack above 20 degrees. Hence, the computational model described above was tested at five angles of attack between 20 and 40 degrees as this range is of particular interest in vertical tail buffet studies.

In all the test cases, the fluid was started impulsively and computation was carried out for 300 time steps with time increment of $\Delta t = 0.012$. Due to the relatively small time increment employed in the solution, the first order convection scheme is considered sufficient. The total computed time interval corresponds to the time to travel 8.6 tail root chord lengths at the rate of the free-stream velocity. It was found during preliminary runs that this computational time is adequate to obtain a fully developed

vortex wake and allow for the unsteady buffet loads to be considered as random and stationary in a statistical sense.

Snapshots of unsteady wake development over delta-wing, vertical-tail configuration after 300 time steps are visualised using particles associated with the wake nodes and presented in Figure 3, Figure 5 and Figure 7 for the 20, 30 and 40 degrees angle of attack, respectively. Here, only the vortex wake which is shed from the wing leading edges is visualised for clarify.

Comparison of the results for all the angles of attack shows a similarity of the vortex wake structures. For every angle of attack, the wakes generated by the delta wing are similar. The major distinction between the wake structures at different angles of attack is the magnitude of the leading edge vortex. It can be noted that the leading edge vortex initially retains its structure over the wing but experiences perturbations and deteriorates when approaching the trailing edge prior to impinging on the vertical tails. In all the cases, the interaction of the leading edge vortical flow with the vertical tails produces a highly disturbed wake, which convects downstream undergoing gradual expansion. Despite the severe degeneration of the vortex wake structure, some periodicity is seen in the formation of vortex clusters.

For more detailed inspection, each of the above plots of the vortex wake is also accompanied by a close view of the leading edge flow, see Figure 4, Figure 6 and Figure 8. On these plots, only one leading edge vortex is visualised by particle traces, which are plotted for several consecutive time steps, forming streaklines. As one can see in Figure 6, for the case of 30-degree angle of attack the vortex model performs well in computing the leading edge vortex roll-up, which is typical of the flow over delta wings. The leading edge vortex expands in a continuous manner as it convects downstream. Its core is initially intact and stable as indicated by coinciding particle traces. However, at approximately 75% cord position the vortex shows signs of instability, and growing scatter of the particle traces reveals sudden enlargement of the vortex size caused by perturbation of its core. It is evident from the plot that the increase of the vortex core size is followed by development of highly diffuse and disorganised vortical flow, which convects downstream and partially covers the region inboard of the twin vertical tails. This rapid degeneration of a well-defined leading edge vortex into a substantially larger, more diffuse vortical flow region meets the criteria of vortex-breakdown provided by O'Neil *et al.* [4].

It can be observed that the twin tails cut through the vortex breakdown flow of the leading edge vortex, splitting it into two vortical flows at each tail, with two vortical flows inside the region between the twin tails and one small vortical flow outside each tail. The vortical flows inside the region are larger but weaker than those outside the twin tails. The smaller outer vortex flow develops above the vertical tail, just outboard of the tail tip. This smaller vortex core moves upward as the flow travels downstream. It is also observed from Figure 6 that interaction of the leading edge vortex breakdown

flow with the vertical tail causes further degeneration of the vortex wake as indicated by highly scattered particle traces.

The leading edge vortex burst becomes more pronounced at the higher angle of attack of 40 degrees, see Figure 8. Here, the computations simulated a leading edge vortex, which is similar to that of the 30-degree case but larger in size, as would be expected. Again, the leading edge vortex expands in a continuous manner as it is convected downstream until a sudden change occurs in its structure and an initially stable vortex starts to deteriorate into an unsteady wake-like flow. As indicated by a progressing scatter in particle traces, this perturbation in the leading edge vortex structure is also suggestive of vortex breakdown. However, at this angle of attack the vortex structure starts to deteriorate earlier at approximately 65% of the chord, producing more severe perturbations of the vortex wake.

Inspection of the leading edge flow at the 20-degree angle of attack in Figure 4 shows that for this case the wake has not deteriorated to the degree found at the higher angles of attack and actually remains stable all the way along the wing. Insignificant scatter in the particle traces indicates only slight perturbation of the leading edge vortex when approaching the trailing edge region that could be triggered by its interaction with the vertical tail. It suggests that for this angle of attack no burst seems to occur or the location of vortex breakdown is very close to the trailing edge.

Based on the results for the angle of attack of 20 degrees and higher, a conclusion can be made that the predicted burst location moves upstream with the increase in the angle of attack. This is consistent with experimentally observed trends of forward shift in the longitudinal location of the vortex burst, see [10,11].

Further investigation into the structure of the leading edge vortex along the wing is performed to verify the occurrence of vortex breakdown. A wing-aligned coordinate system is chosen to facilitate the investigation. With the origin at the wing's apex, the *X*-axis is taken to be along the wing's cord, the *Z*-axis lies in the wing-normal plane containing the *X*-axis, and the *Y*-axis is parallel to the wing surface and pointing outboard. Following the initial assumption of flow symmetry, only half of the flow structure is assessed. Thus, cross-sections of the leading-edge vortex are taken in the *Y-Z* plane in several chordwise locations to examine the region of vortex perturbation, see Figure 9 to Figure 14. Note, that the vertical tail leading edge is located at x=1.0 and its trailing edge is at x=1.4.

Contour plots of time-averaged chordwise velocity for several cross flow planes along the wing chord are shown in Figure 11 for the 30-degree case. The existence of breakdown is indicated by the drop in the magnitude of the axial velocity along the vortex core and rapidly developing region of flow deceleration. The breakdown of the leading edge vortex core is located forward of the wing trailing edge at about x=0.75, which is consistent with the results of Washburn *et al.* [15].

Contour plots of chordwise velocity fluctuations are also presented in Figure 12 for the 30 degrees angle of attack. As indicated by the results, the flow is steady upstream of the supposed breakdown location but the presence of velocity fluctuations further downstream indicates the onset of vortex burst. It can be noted from the plots that in the vortex breakdown flow, the magnitude of the velocity fluctuations decreases gradually towards the edges of the flow. This is not in agreement with the results of Lee and Brown [38], who concluded that the total pressure fluctuations in the vortex breakdown flow are decreasing towards the vortex core.

Inspection of the mean and RMS chordwise velocity plots shows that for all angles of attack, the location of vortex breakdown of the wing leading-edge cores is forward of the wing trailing edge. The vortex breakdown flow becomes larger in size and moves upward as it travels downstream. It is evident that the increase in the angle of attack changes the location and shape of the vortex breakdown flow on the wing and between the twin tails. In all the cases, the position of the time-averaged centre of breakdown flow is totally inside the region between the twin tails. For the higher angles of attack, the area occupied by the breakdown flow becomes larger in size and moves closer to the tail. Also, a small vortical flow region is present at the outboard side of the tail's tip and it tends to shift upwards for higher angles of attack.

Figure 15 shows a three-dimensional view of the iso-surfaces of time-averaged pressure coefficient for the delta-wing, vertical-tail configuration at 30 degrees angle of attack. It is observed from the figure that the centre of the vortex breakdown flow is located inboard of the vertical tail which is in agreement with the predictions of Kandil *et al.* [14]. The area of vortex breakdown becomes larger in size as it approaches the vertical tail and the decelerated flow starts to recover just after it passes the wing's trailing edge. Figure 16 shows that for the 40 degree angle of attack, the vortex-breakdown flow is still inside the region between the twin tails and experiencing more intense breakdown compared to the results obtained of 30 degree angle of attack.

4.3.2 Differential Pressure Distribution on a Vertical Tail

One of the important characteristics of tail buffet is the magnitude and frequency of instantaneous pressure fluctuations on the tail surface. Many experimental publications reported information about the surface pressure fluctuations measured at 45% chord and 60% span location at the vertical tail. A pressure transducer was installed at this point on the vertical tail in most of the tests to ensure that the results have a common point for comparison.

A computed time history of the differential pressure fluctuation at 45% chord and 60% span location on vertical tail at 30-degree angle of attack is presented in Figure 17. The instantaneous values of differential pressure are obtained as the difference between the inboard and outboard pressures on the vertical tail. The unsteady pressure fluctuations

are clearly cyclic and oscillate about a local apparent mean value. The results calculated at this particular location appear to be typical of the pressure variation at any other location on the tail.

Computed time histories of differential pressure coefficient at both the tip and root locations are shown in Figure 18 for 30 degrees angle of attack. Comparison shows a distinct difference between the flow at the tip and root locations where both the means and amplitudes are quite different. Another feature of the computed differential pressures time histories for the tip and root locations is the presence of fluctuations, which are 180 degrees out of phase. Here, the tip differential pressure is increasing while the root value is decreasing and *vice versa*, creating a load distribution that has the potential to excite the tail's higher order modes of vibration. Further investigation revealed that this feature is essentially true at any other angle of attack.

As can be seen from the above results, the differential pressure coefficient fluctuates substantially and exhibits oscillatory motion with random fluctuations sometimes of large magnitude compared with the mean value. Such behaviour of the buffet loads is determined by interaction of the degenerated leading edge vorticity with the vortex system of the twin vertical tails. The presence of a stagnation zone in the vortex breakdown flow causes the leading edge vorticity to concentrate in the region between the twin tails, gradually building up a vortex cloud. The process of formation and destruction of the vortex clouds of different signs interacting with the tail vortex system drives the oscillatory behaviour of the buffet loads. The periodicity of the vortex cloud formation determines the dominant frequency of buffeting flow. These drifting clouds of arbitrarily scattered vortex elements are also subjected to random-like motion caused by vortices bouncing back off the wall. As a result, the surface vorticity and, therefore, the pressure distribution on the wall are also subject to some degree of randomness. This can be referred to as numerical noise since it is completely caused by spatial discretisation involved in vortex dynamics.

For the analysis of time-dependent data influenced by a certain degree of randomness, the steady and fluctuating features of the flow are defined by using statistical data reduction, see, for example, Pettit *et al.* [36]. This allows for proper comparison between theory and experiment for the purposes of validation. Assessment of the buffet pressure history in Figure 17 suggests that the pressure fluctuations can be classified as a random stationary process subject to standard analysis techniques in the time and frequency domains. Thus, the values of unsteady differential pressures can be integrated over the vertical tail surface to give steady and fluctuating components of aerodynamic load coefficients. The unsteady pressure and loads coefficients can be reduced to root-mean-square (RMS) and power spectral density (PSD) forms. The peak power and the dominant frequency of the unsteady buffet loads can be determined from their PSD plots.

4.3.2.1 Time-averaged Buffet Pressures

The mean static pressure $\overline{P}(\mathbf{r})$ at the body surface is obtained by averaging the buffet pressure history over a specified elapsed time $t_e - t_s$ as follows

$$\overline{P}(\mathbf{r}) = \frac{1}{t_e - t_s} \int_{t_s}^{t_e} P(\mathbf{r}, t)\, dt, \tag{63}$$

where the values for start t_s and end t_e of sampling are selected as 1.4 and 8.6, respectively, for all the cases where time averaging was required.

Thus, the steady pressure coefficient at the body surface is defined as

$$\overline{C}_P(\mathbf{r}) = (\overline{P}(\mathbf{r}) - P_\infty)/q_\infty, \tag{64}$$

where q_∞ is the free-stream dynamic pressure.

Time histories of differential pressure at the vertical tail are computed by subtracting the outer surface pressure values from the inner surface pressure values. Therefore, steady differential pressure coefficient $\overline{C}_{\Delta P}(\mathbf{r})$ at the vertical tail surface can be determined as

$$\overline{C}_{\Delta P}(\mathbf{r}) = \frac{1}{(t_e - t_s)\, q_\infty} \int_{t_s}^{t_e} (P_{in}(\mathbf{r}) - P_{out}(\mathbf{r}))\, dt = (\overline{P}_{in}(\mathbf{r}) - \overline{P}_{out}(\mathbf{r}))/q_\infty. \tag{65}$$

Here, a positive pressure difference across the vertical tail corresponds to a net load acting outboard.

Contour plots of time-averaged differential pressure coefficients on the vertical tail are presented in Figure 19 through Figure 21 for three values of angle of attack to show its effect on pressure distribution over the tail. As one can see, at any angle of attack the differential pressure values are positive for most of the tail surface, indicating an outboard-directed net force. The only exception is an area along the trailing edge near the root where negative values of differential pressure corresponds to inboard-directed force for all the test conditions.

The locations of the regions of maximum and minimum mean differential pressure at these three values of incidence are quite similar. The most positive differential pressure is found near the leading edge close to the tail's root, and the most negative differential pressure is found close to the trailing edge near the root. Unlike the positive differential pressures on the tail, the peak of the negative differential pressure tends to decrease at higher angles of attack.

The magnitude of the mean differential pressure gradually decreases towards the trailing edge in chordwise direction. This is not in agreement with the trends found in full-scale experimental data [36] where the mean differential pressure tended to decrease both in chordwise and spanwise directions.

Near the root, the mean differential pressure is higher than that on the rest of the tail with the largest values being detected near the leading edge. The largest gradients of the time-averaged differential pressures are also detected near the tail root and in the leading edge area. For the rest of the tail surface, the mean differential pressure values are changing evenly with the larger gradients in the vertical tail's aft tip area. This pattern of mean differential pressure distribution along the tail surface is found to be similar for all the angles of attack with the larger mean values corresponding to the higher angles of attack.

4.3.2.2 RMS Pressure Distribution

The time-averaged fluctuating component $P'(\mathbf{r})$ of unsteady pressure on the body surface may be found as the root-mean-square (RMS) of the zero-mean, instantaneous buffet pressure

$$P'^2(\mathbf{r}) = \frac{1}{t_e - t_s}\int_{t_s}^{t_e}(P(\mathbf{r},t) - \overline{P}(\mathbf{r}))^2\, dt. \tag{66}$$

Similarly, the zero-mean RMS differential buffet pressure $\Delta P'(\mathbf{r})$ at the vertical tail, which provides a measure of the average fluctuations of the unsteady net pressure, is determined as

$$\Delta P'^2(\mathbf{r}) = \frac{1}{t_e - t_s}\int_{t_s}^{t_e}(P_{in}(\mathbf{r},t) - P_{out}(\mathbf{r},t))^2\, dt, \tag{67}$$

and the RMS differential pressure coefficient is then defined as

$$C'_{\Delta P}(\mathbf{r}) = \Delta P'(\mathbf{r}) / q_\infty, \tag{68}$$

Contour plots of the RMS differential pressure fluctuations on the vertical tail are presented in Figure 19,Figure 20 and Figure 21. The magnitude of RMS differential pressure in most of the locations increases with the increase of angle of attack, where location of vortex breakdown tends to move upstream of the tails. Close to the leading edge of the tail, the pressure fluctuations are higher and they decrease towards the trailing edge. However, for 40 degrees angles of attack, a decrease in differential pressure is found only in a region extending from the leading edge to approximately 50% chord. The highest RMS differential pressure is found near the leading edge close to the tail's root. This increase in RMS value of unsteady pressure fluctuations near the leading edge and root cannot be confirmed from the experimental data since no pressure taps were located in those areas.

In general, a pattern of the intensity of the unsteady pressure fluctuations is similar for 20 and 30 degrees angles of attack, with some changes appearing for the higher values of incidence. The position of the centre of the vortex breakdown flow accounts for the behaviour of the pressure fluctuations observed in the plots. Thus, at an angle of attack of 20 degrees, the lower half of the tails experience larger RMS pressure levels than those on the rest of the tail. At 40 degrees angle of attack, the distribution of the differential pressures is more even in the spanwise direction for the whole surface of the tail.

At 20 degrees angle of attack, the magnitude of the RMS differential pressure gradually decreases towards the trailing edge in the chordwise direction and towards the tail tip in spanwise direction. This variation of the differential RMS pressure over the vertical tail agreed qualitatively with the full-scale experimental data of Pettit *et al.* [36], although the measured RMS values were lower than those obtained in the computation for most of the vertical tail. However, at 40 degrees angle of attack, the magnitude of the RMS differential pressure decreases towards the trailing edge mainly in the chordwise direction.

The computational results indicate that an increase in the angle of attack intensified tail buffet by increasing the RMS levels of differential pressure fluctuations and expanded the region of the peak loading from the root of the tail toward the leading edge and centre of the tail.

4.3.2.3 Power Spectral Density of Buffet Pressures

Another characteristic of interest is the power spectral density function of the unsteady component of the differential pressure coefficient denoted as $C''_{\Delta P}$. The differential pressure time histories from each test condition were converted into the frequency domain using Fast Fourier Transform (FFT) techniques. The length of the computed time histories was 8.6 based on tail root chord. The time histories were divided into blocks, each containing 48 samples and the Hanning window was applied to reduce bandwidth leakage. The average PSD functions were obtained by averaging the fast Fourier transforms of each of the blocks, and an average of 9 transforms with 50% overlap was used to increase statistical confidence. The dominant frequencies f of the buffet loads were identified from the power spectral density plots where the dimensionless frequency resolution was 0.73 based on the tail's root chord.

Figure 22 shows the variation in the spectral content of the differential pressure fluctuations with angle of attack at the 45% chord, 60% span location. The differential pressure spectra show that for all the angles of attack the pressure field contains energy over a moderately wide frequency range. At 20 degrees angle of attack the peak in the buffet power spectrum is relatively small. However, the peak becomes progressively sharper and stronger as the angle of attack is increased. This indicates a concentration

of the buffet energy in an increasingly narrow frequency band that is accompanied by higher peak buffet levels. This trend is consistent with full-scale experimental data [36].

Examination of the PSD plots in Figure 22 indicates a presence of several dominant frequencies in the surface pressure fluctuations where most of the buffet energy is concentrated in two peaks having narrowly separated frequencies of 0.73 and 2.9. Also, the shape of the plot indicates a possible presence of the third peak at 6.6. However, a higher resolution in the PSD plot is required to identify the true location of the peaks.

As one can see, the variation of dominant frequencies on the tail with angle of attack has some definite trends. Results for 20 degrees angle of attack show a main peak of pressure power to be at approximately 2.9 and a lower peak value at about 0.73. For the 30-degree angle of attack, the power spectral density plot shows a clear increase of the peak pressure power at 0.73 and a major peak at the dominant frequency of 2.9, which became stronger and more distinct compared to the 20-degree case. In the case of 40 degrees angle of attack, two separate distinguishable frequencies can be identified in the power spectral density plot with the peak pressure power value at 0.73 starting to dominate over the magnitude of the second peak at 2.9.

The non-dimensional form of the buffet excitation spectrum as suggested by Mabey [39] may be expressed in terms of the free-stream dynamic pressure as

$$\left(\frac{P'(\mathbf{r})}{q_\infty}\right)^2 = \int_{n=0}^{n=\infty} F(n)dn = \int_{\ln n=-\infty}^{\ln n=+\infty} nF(n)d(\ln n), \tag{69}$$

where $F(n)$ is the non-dimensional power spectral density of buffet pressure fluctuations and is essentially a PSD of unsteady pressure coefficient $C_{\Delta P}(\mathbf{r})$. The reduced frequency n may be expressed as the Strouhal number of differential pressure fluctuations

$$n = \frac{f\bar{c}}{U_\infty}, \tag{70}$$

based on a characteristic length $\bar{c}$ of tail's root chord.

Following recommendations from Mabey, the computed buffet pressure spectra plots are also presented as $\sqrt{nF(n)}$ versus reduced frequency n, see Figure 23. As one can see, this form of the buffet pressure spectral density emphasises the significance of higher harmonics in the power spectrum. Thus, the domination of the peak pressure power at a frequency of 6.5 is highlighted for the 20-degree case and at 2.9 for the 30 and 40-degree cases.

The trends described above regarding the power spectral density of the differential pressure coefficient for the 45% chord, 60% span location for different angles of attack

appears to be representative of the spectral contents for the majority of other locations on the tail. The differential pressure power peaks occur at almost constant frequency values across the whole tail surface. In the case of peak differential pressure power, the values increase over most of the tail with increase in the angle of attack, which is consistent with available experimental results [11,35]. The decrease of dominant frequency of pressure fluctuations at higher angles of attack is also in agreement with experimentally observed trends.

However, the vortex model failed to predict the characteristic frequency of the pressure fluctuations in the flow past a burst vortex as the dominant frequency of about 0.5 was identified in most of the sub-scale and full-scale experiments on F/A-18 tail buffet. This discrepancy in prediction may be caused by the coarseness of the vorticity spatial discretisation in the region close to the leading edge vortex burst. It is known from experimental studies that the peak in the buffet pressure spectra is a property of the flowfield of the burst LEX vortex and is not caused by structural effects related to its interactions with the vertical tails. Therefore, its centre frequency is associated with some characteristic frequency present in the flowfield generated as a result of the LEX vortex bursting. However, up until now, there is no theory on the mechanism of how such a discrete frequency can be generated. Further numerical investigation of the vortex model is required to explain the reason for the above discrepancy. Also, increasing the length of the computed time histories is required to improve the resolution of the predicted buffet pressure characteristics.

4.3.3 Vertical Tail Buffet Loads

The unsteady differential pressures were integrated over the tail surface in a piecewise constant manner to obtain the instantaneous normal force and root bending moment coefficients. The time history of the unsteady normal force coefficient was determined according to

$$C_N(t) = \frac{1}{q_\infty A_F} \sum_i (P_{in}(\mathbf{r}_i, t) - P_{out}(\mathbf{r}_i, t)) A_i = \frac{1}{A_F} \sum_i C_{\Delta P}(\mathbf{r}_i, t) A_i, \qquad (71)$$

where A_F is the total planform area of the tail, A_i is the area of the i-th panel on the tail and the instantaneous pressure differential $C_{\Delta P}$ is evaluated in the middle of the i-th panel. The surface pressure over the panel area was assumed to be constant and equal to the pressure computed at the centre of the panel.

The unsteady root bending moment was evaluated in a similar manner, assuming that the resultant force over the i-th panel is acting at the panel's centroid

$$C_{BM}(t) = \frac{1}{q_\infty A_F c_F} \sum_i (P_{in}(\mathbf{r}_i, t) - P_{out}(\mathbf{r}_i, t)) A_i l_i = \frac{1}{A_F c_F} \sum_i C_{\Delta P}(\mathbf{r}_i, t) A_i l_i, \qquad (72)$$

where c_F is the tail's root chord and l_i is the distance from the tail's root to the centroid of the i-th panel. Here, a bending moment directed toward outboard is considered positive.

In the present study, the tail's root chord c_F is selected as the characteristic length to maintain consistency with the results of previous numerical investigations of delta-wing, vertical-tail configurations. However, in some of the previous sub-scale and full-scale experimental investigations of F/A-18 vertical tail buffet, the wing's mean aerodynamic chord of 11.54 *ft* was selected as the characteristic length, rather than tail's root chord of 9.42 *ft*.

The steady components of the fluctuating normal force and root bending moment coefficients are determined from their time histories as

$$\overline{C}_N = \frac{1}{t_e - t_s} \int_{t_s}^{t_e} C_N(t)\, dt, \tag{73}$$

and

$$\overline{C}_{BM} = \frac{1}{t_e - t_s} \int_{t_s}^{t_e} C_{BM}(t)\, dt. \tag{74}$$

Similarly, the zero-mean RMS values of fluctuating normal force and root bending moment coefficients, which provides a measure of the average fluctuations of the unsteady buffet loads at the vertical tail are determined as

$$C_N'^2 = \frac{1}{t_e - t_s} \int_{t_s}^{t_e} (C_N - \overline{C}_N)^2(t)\, dt, \tag{75}$$

and

$$C_{BM}'^2 = \frac{1}{t_e - t_s} \int_{t_s}^{t_e} (C_{BM} - \overline{C}_{BM})^2(t)\, dt, \tag{76}$$

respectively.

The variations of time-averaged and RMS normal force coefficients as a function of angle of attack are presented in Figure 24 and Figure 25, respectively, and compared with full-scale experimental data of [36]. The variation of time-averaged and RMS root bending moment coefficients at different angles of attack are also presented in Figure 26 and Figure 27 and compared with the experimental data. It may be noted that both the experimental and computational data indicate a substantial positive loading on the

vertical tail, which is caused by the local angle of attack distribution on the tail generated by the upstream flow separation from the wing's leading edge.

The computed and experimental mean values of both the normal force and moment increase with the angle of attack. This is caused by the variation of the peak steady pressure locations on the tail as the angle of attack is increased, since the leading edge vortex passes closer to the tail's tip at higher angles of attack. The contour plots of the mean differential pressure at the vertical tail also show a higher levels of differential pressure as angle of attack is increased, see Figure 20 and Figure 21.

Although the time-averaged buffet loads predicted by the vortex model follow the same trend as the experimental data, a quantitative agreement between them is marginal. Figure 24 and Figure 26 show that computations tend to substantially over-predict the mean normal force and bending moment for the whole range of angles of attack.

Comparison of the computed and experimental RMS normal forces and bending moments in Figure 25 and Figure 27 shows that computations produce values which are reasonably close to those measured during full-scale test. Initially, both the computed and measured values of RMS buffet loads follow similar trends and increase with the angle of attack. However, the vortex model fails to follow the experimentally obtained trend for angles of attack of 30 degrees and higher. As one can see, the peak of the experimentally measured RMS buffet loads is reached by 32 degrees of angle of attack after which its value starts to decline. Meanwhile, the predicted RMS buffet loads experience a local minimum at 30 degrees but then continue to increase at higher angles of attack.

Power spectral density functions of the unsteady buffet loads are determined from their time histories in a manner similar to the buffet pressures PSD and presented in Figure 28 and Figure 29 for normal force and root bending moment coefficients, respectively. The peaks in the power spectral density plots can be detected for all the three angles of attack investigated. It may be noted that the dominant frequencies at which the normal force and bending moment are exerted on the vertical tail tend to decrease at higher angles of attack. However, their variation at lower angles of attack has less definite trends.

5. Conclusions

A computational simulation of vertical tail buffet was performed using an unsteady vortex filament method. The computational model consisted of a 76-degree sharp-edged delta wing along with F/A-18 twin vertical tails, which were placed aft of

the wing. This delta-wing, twin-tail configuration was analysed at flow conditions and angles of attack known to produce an unsteady vortex breakdown flow.

The results of numerical simulation are presented for 20, 30 and 40 degrees angle of attack as this range is of particular interest in vertical tail buffet studies. For angles of attack above 20 degrees, the unsteady vortex method produced a perturbation in the leading edge vortex that resulted in degeneration of the well-defined vortex structure into a larger and more diffuse vortical flow region. It indicated the existence of vortex burst, and was further confirmed by inspection of flow field characteristics in the vortex breakdown area. It was found that the predicted location of the vortex burst moves upstream at higher angles of attack which is consistent with experimentally observed trends.

It was shown that the numerical solution is able to predict, with some limitations, the development of unsteady buffet loads on the vertical tail produced by the vortex breakdown flow. A comparison of computational results with available full-scale wind-tunnel data on F/A-18 tail buffet showed that the vortex model did a reasonable job in simulating the spatial and temporal characteristics of the buffet loads. Comparisons were made in terms of time-averaged differential pressures and loads as well as the root-mean-square values of both quantities. It was found that computation is able to simulate both the local unsteadiness at a specific point on the tail, such as differential pressure, as well as the global unsteadiness, such as tail buffet loads.

Although there were large discrepancies between the computed and experimental values of time-averaged differential pressures, the RMS values of fluctuating differential pressures and their distributions over the tail compared fairly well with the experimental data. Computational results indicated that the RMS levels of differential pressure fluctuations increase with the angle of attack which is also in agreement with the trends observed in full-scale experiments.

Analysis of power spectral density of predicted differential pressures on the tail indicated that their dominant frequencies are higher compared to experimentally measured values. Despite the discrepancy in predicted values of buffet pressure dominant frequency, the variation of buffet loads with the angle of attack is predicted with reasonably good accuracy. Numerical solutions showed that for most of the angles of attack investigated, the predicted RMS normal force and bending moment are in good agreement with the experimental data both qualitatively and quantitatively. Time-averaged normal force and bending moment predicted by the vortex model follow the same trends as the experimental data, and quantitative agreement between them is encouraging.

Numerical solutions showed that despite some discrepancies in predictions, such important tail buffet characteristics as RMS values of fluctuating pressures and loads as well as the trends of their variation with the angle of attack are in qualitative agreement with the experimental data. It shows that complex unsteady problems such

as vertical tail buffet due to leading edge vortex burst can be modelled reasonably well by computationally inexpensive vortex methods. It should be noted that no assessment of the effects of compressibility or wake diffusion on the computational results was made in the present study. However, within the range of flight conditions where the F/A-18 vertical tail buffet occurs their contribution is expected to be insignificant.

Predictive capabilities of the vortex model can be refined by increasing the vorticity spatial resolution in sensitive regions, such as the area of the vortex burst. The higher density of vortex elements and use of disconnected vector-valued vortex particles for representation of the leading edge vorticity will add to the computational expense, but should be explored to determine its benefits. The use of finer spatial discretisation of the leading edge vortex near the burst location will improve the resolution of the unsteadiness aft of the vortex burst point. This in turn may result in more accurate predictions of instantaneous values and spectral content of unsteady buffet loads on the vertical tail. This is being considered for future studies.

References

1. Peckham, D.H., Atkinson, S.A. (1957) *Preliminary Results of Low Speed Wind Tunnel Tests on a Gothic Wing of Aspect Ratio 1.0*, ARC CP508.
2. Benjamin, T.B. (1962) Theory of the Vortex Breakdown Phenomenon, *J. Fluid Mech.*, Volume 14, pp. 593-629.
3. Ekaterinaris, J.A., Schiff, L.B. (1990) Vortical Flows over Delta Wings and Numerical Prediction of Vortex Breakdown, *AIAA 28th Aerospace Sciences Meeting*, 90-0102, pp. 1-22.
4. O'Neil, P.J. and others, (1989) Numerical Simulation of Leding-Edge Vortex Breakdown Using an Euler Code, *AIAA 7th Applied Aerodynamics Conference*, 89-2189-CP, pp. 218-226.
5. Midkavi, V.Y. (1994) Computation of Vortex Breakdown, *CFD: Advances and Applications*, pp. 241-280.
6. Lopez, J.M. (1990) Axisymmetric Vortex Breakdown Part 1. Confined Swirling Flow, *Journal of Fluid Mechanics*, 221:533-552.
7. Brown, G.L., Lopez, J.M. (1990) Axisymmetric Vortex Breakdown Part 1. Physical Mechanisms, *Journal of Fluid Mechanics*, 221:553-576.
8. Thompson, D.H. (1975) *A water tunnel study of vortex breakdown over wings with highly swept leading edges*, Aeronautical Research Laboratory, Aerodynamics Note 356.
9. Thompson, D.H. (1985) *A visualization study of the vortex flow around double-delta wings*, Aeronautical Research Laboratory, Aerodynamics Report 165.
10. Thompson, D.H. (1990) *Water tunnel flow visualization of vortex breakdown over the F/A-18*, Aeronautical Research Laboratory, Flight Mechanics Report 179.

11. Martin, C.A., Thompson, D.H. (1991) Scale Model Measurements of Fin Buffet Due to Vortex Bursting on F/A-18, *AGARD Manoeuvring Aerodynamics*, AGARD-CP-497.
12. Thompson, D.H. (1997) *Effect of the Leading Edge Extension (LEX) Fence on the Vortex Structure over the F/A-18*, Aeronautical and Maritime Research Laboratory, DSTO-TP-0489.
13. Hitzel, S.M. (1988) Wing Vortex - Flows Up Into Vortex Breakdown - A Numerical Simulation, *AIAA 6th Applied Aerodynamics Conference*, 88-2518-CP, pp. 73-83.
14. Kandil, O.A., Sheta, E.F., Massey, S.J. (1996) Twin Tail/Delta Wing Configuration Buffet due to Unsteady Vortex Breakdown Flow, AIAA Paper 96-2517-CP.
15. Washburn, A.E., Jenkins, L.N., Ferman, M.A. (1993) Experimental Investigation of Vortex-Fin Interaction, AIAA Paper 93-0050, Reno, NV.
16. Nakamura, Y., Leonard, A., Spalart, P.R. (1983) Numerical Simulation of Vortex Breakdown by the Vortex Filament Method, *AGARD Aerodynamics of Vortical Flows in Three Dimensions*, SEE N84-12099-03-02.
17. Lorey, D.A. (1991) *Vortex Bursting over a Unit Area Aspect Ratio Wing Using Vortex Panelling Methods*, Thesis, Air Force Institute of Technology, WPAFB OH 45433-6583.
18. Helmholtz, H. (1867) On Integrals of the Hydrodynamic Equations which Express Vortex-Motion, Translation of P. G. Tait, in *Phil. Mag.* (4), Vol 33, 485-512.
19. Leonard, A. (1980) Vortex Methods for Flow Simulation. *J. Comp Phys.* 37, No. 3, 289-335.
20. Lewis, R.I. (1986) The vorticity method - a natural approach to flow modelling. Keynote address to the *International Seminar on Engineering Applications of the Surface and Cloud Vorticity Methods*, Wroclaw, Poland, Vol.46, No. 9, 1-36.
21. Martensen, E. (1959) Berechnung der Druckverteilung an Gitterprofilen in ebener Potentialstromung mit einer Fredholmschen Integralgleichung, *Arch. Rat. Mech., Anal.* 3, 235-270.
22. Belotserkovskii, S.M., Nisht, M.I. (1978) Modelling of Turbulent Wakes in Ideal Fluids (Separated Flow Over Bluff Bodies), *Fluid Mech.-Research*, Vol.7, No. 1, 102-115.
23. Lamb, H. (1945) *Hydrodynamics*, Cambridge University Press.
24. Chorin, A.J. (1973) Numerical study of slightly viscous flows, *J. Fluid Mech.*, 57, 785-796.
25. Chorin, A.J. (1978) Vortex sheet approximation of boundary layers, *J. Comp. Phys.*, Vol. 27, 428-442.
26. Batchelor, J.K. (1970) *An Introduction to Fluid Dynamics*, Cambridge University Press.
27. Rosenhead, L. (1931) The Formation of Vortices from a Surface of Discontinuity, *Proc. Roy. Soc*, Series A, Vol.134, 170-192.
28. Kuwahara, K., Takami, H. (1973) Numerical Studies of Two-Dimensional Vortex Motion by a System of a Point Vortices, *J. Phys. Soc. Japan*, Vol. 34, 247-253.
29. Milinazzo, F., Saffman, P.G. (1977) The Calculation of Low Reynolds Number Two-Dimensional Flow Using Discrete Vortices with Random Walk, *J. Comput Phys.*, Vol. 23, 360-392.
30. Hald, O.H. (1979) Convergence of Vortex Methods for Euler's Equation, *SIAM J. Numer. Anal.*, Vol. 16, 726-755.

31. Leonard, A. (1985) Computing three-dimensional incompressible flows with vortex elements, *Ann. Rev. Fluid Mech.*, Vol. 17, 523-559.
32. Beale, J.T., Majda, A. (1985) High Order Accurate Vortex Methods with Explicit Velocity Kernels, *J. Comput. Phys.*, Vol. 58, 188-208.
33. Chang, C. (1988) Random Vortex Methods for the Navier-Stokes Equations, *J. Comput. Phys.*, Vol. 76, 281-300.
34. Levinski, O.P. (1997) *Vortex Modelling in Unsteady Aerodynamics*, PhD Thesis, Department of Mechanical and Manufacturing Engineering, The University of Melbourne, Australia.
35. Lewis, R.I. (1991) *Vortex element methods for fluid dynamic analysis of engineering systems*, Cambridge University Press.
36. Pettit C.L., Brown D.L., and Pendleton E. (1994) Wind Tunnel Tests of Full-Scale F/A-18 Twin Tail Buffet: A Summary of Pressure and Response Measurements, AIAA Paper 94-3476.
37. James, K.D., Meyn, L.A. (1994) Dependence of Integrated Vertical-Tail Buffet Loads for F/A-18 on Sensor Density, Society of Automotive Engineers, Paper 941140.
38. Lee, B.H., Brown, D. (1990) Wind-Tunnel Studies of F/A-18 Tail Buffet, *J. Aircraft*, Vol. 29, No. 1, 146-152.
39. Mabey, D. (1987) Some Aspects of Aircraft Dynamic Loads Due to Flow Separation, AGARD-R-750.

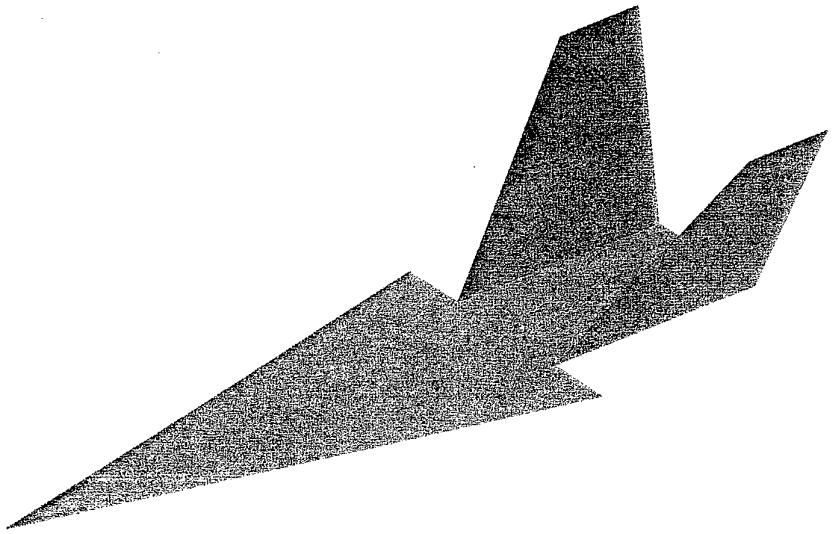

Figure 1 General view of delta wing-twin vertical tail configuration.

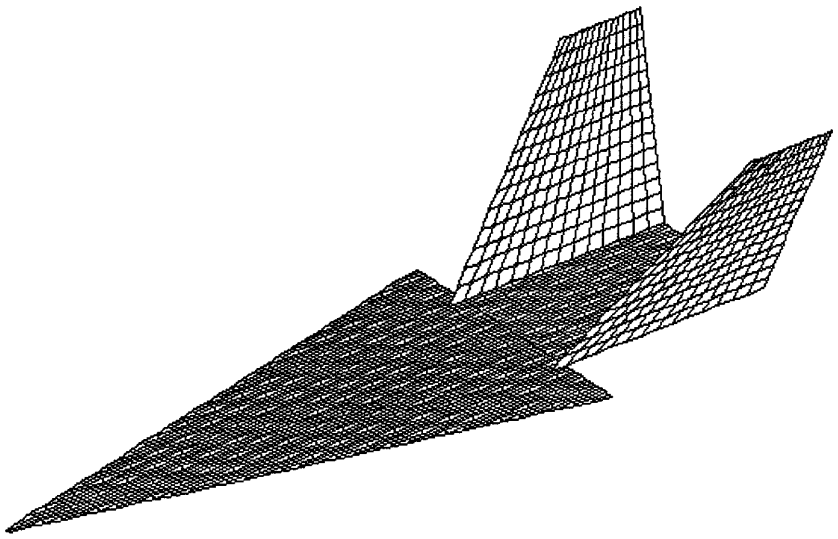

Figure 2 Spatial discretisation of the computational model.

Figure 3 Top view of vortex wake past delta wing with twin tails at 20 degrees angle of attack

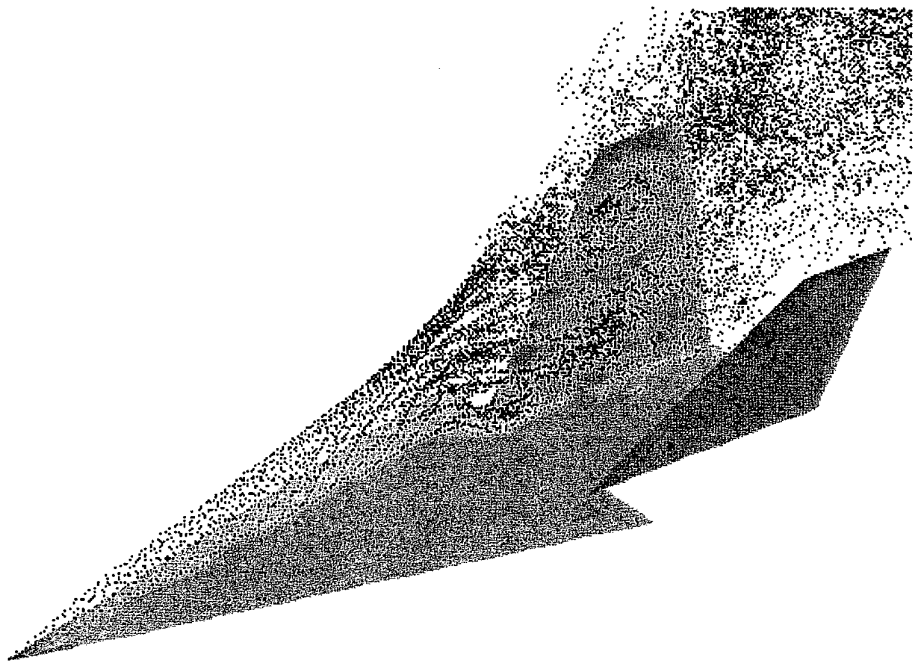

Figure 4 Particle traces of the leading edge vortex core at 20 degrees angle of attack

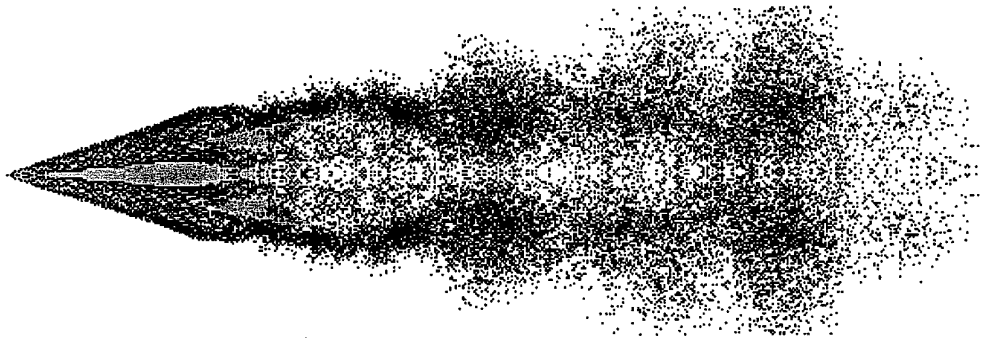

Figure 5 Top view of vortex wake past delta wing with twin tails at 30 degrees angle of attack

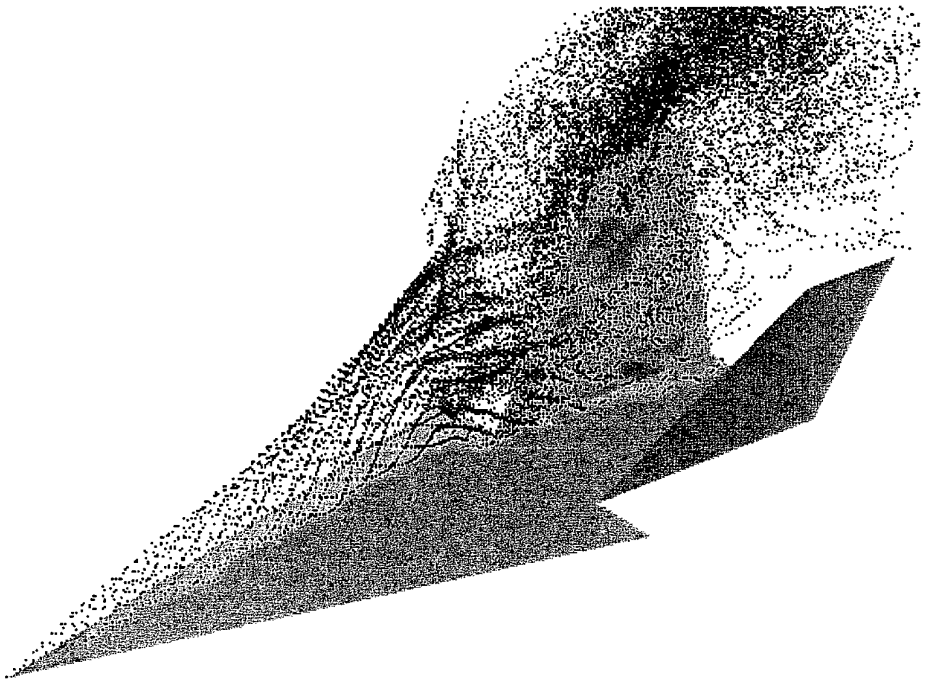

Figure 6 Particle traces of the leading edge vortex core at 30 degrees angle of attack

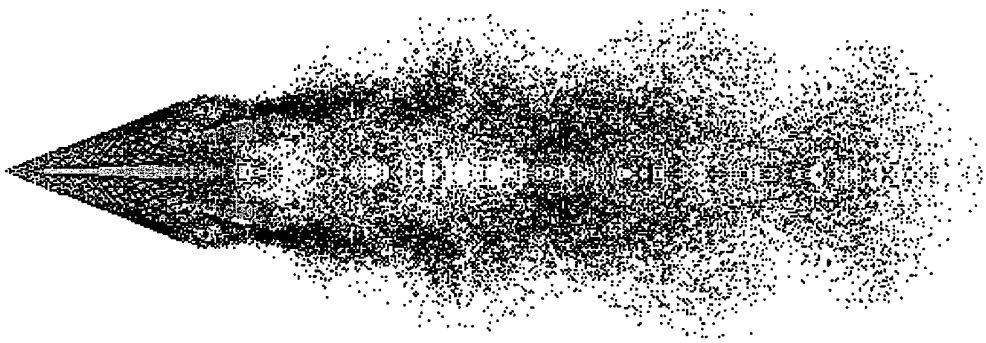

Figure 7 Top view of vortex wake past delta wing with twin tails at 40 degrees angle of attack

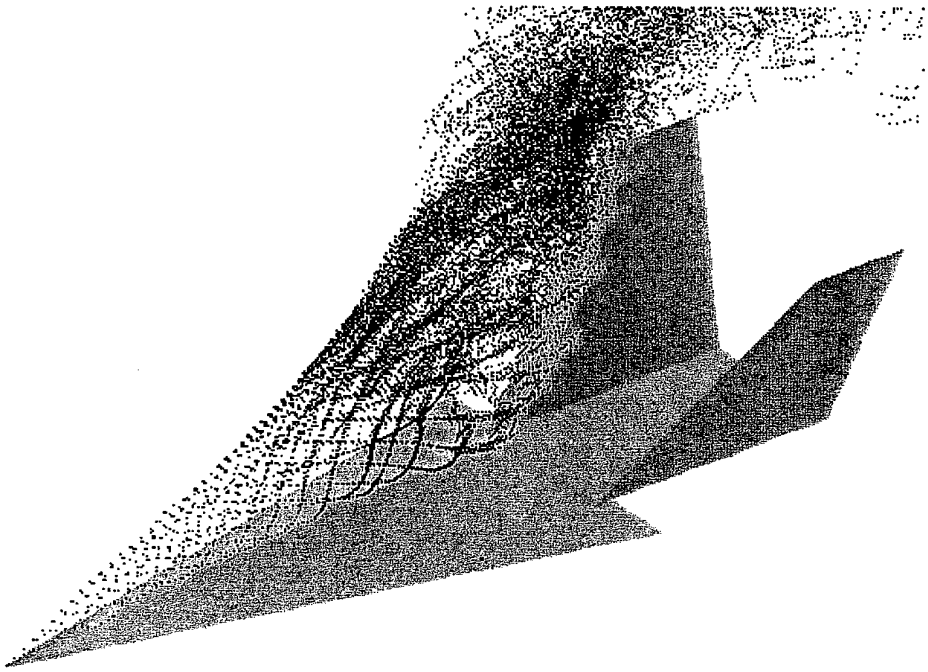

Figure 8 Particle traces of the leading edge vortex core at 40 degrees angle of attack

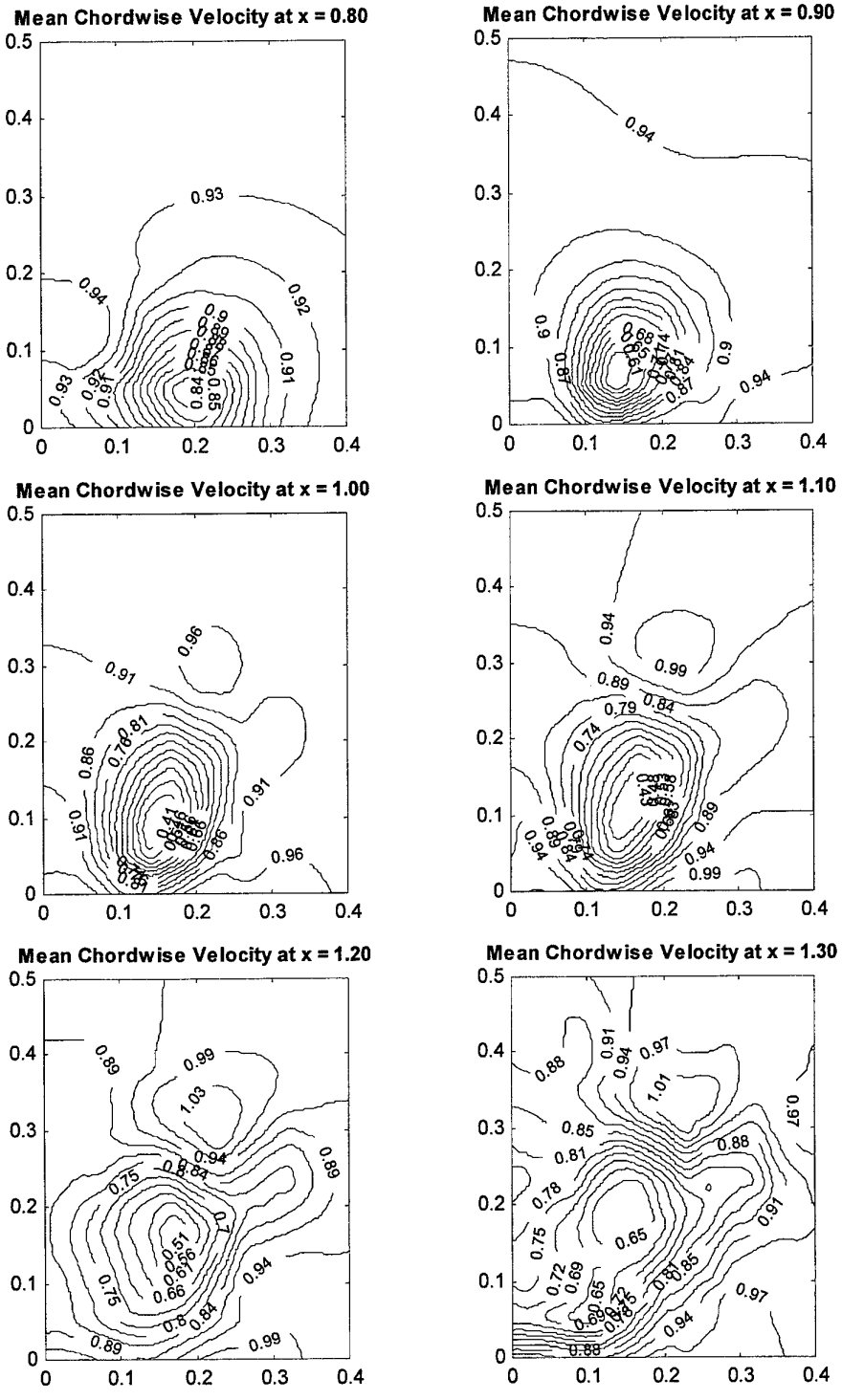

Figure 9 Distribution of mean chordwise velocities at 20 degrees angle of attack.

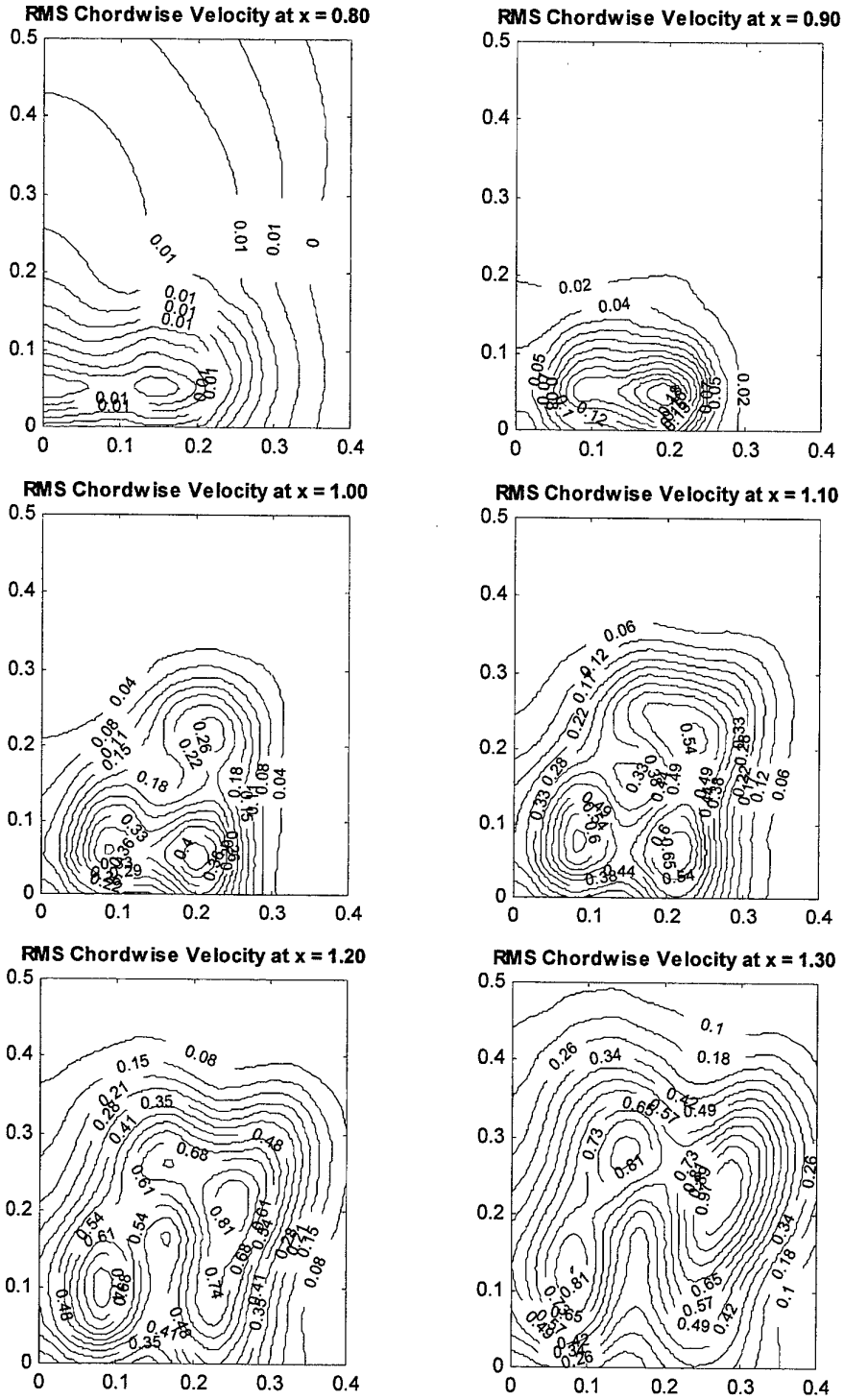

Figure 10 Distribution of RMS chordwise velocities at 20 degrees angle of attack.

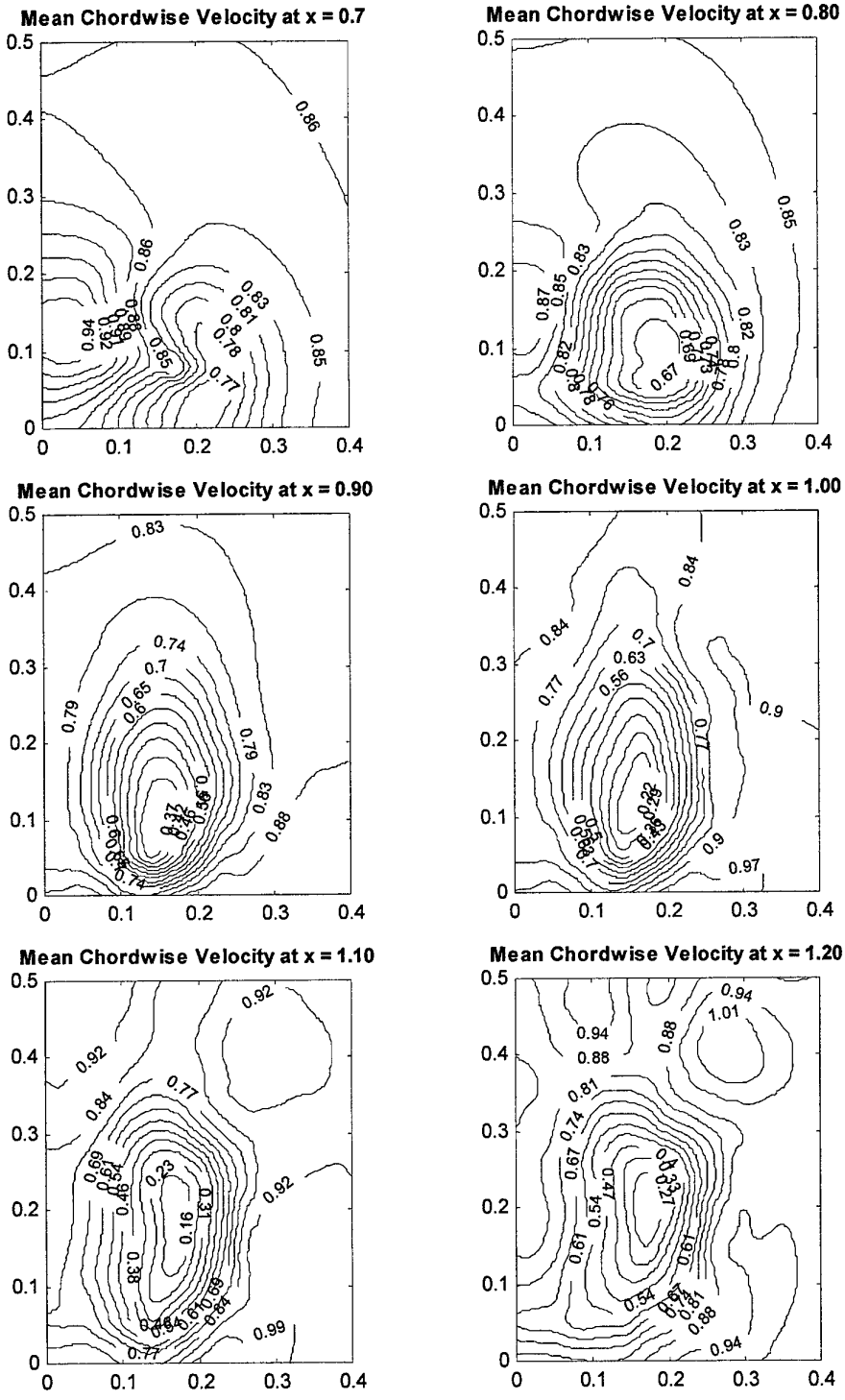

Figure 11 Distribution of mean chordwise velocities at 30 degrees angle of attack.

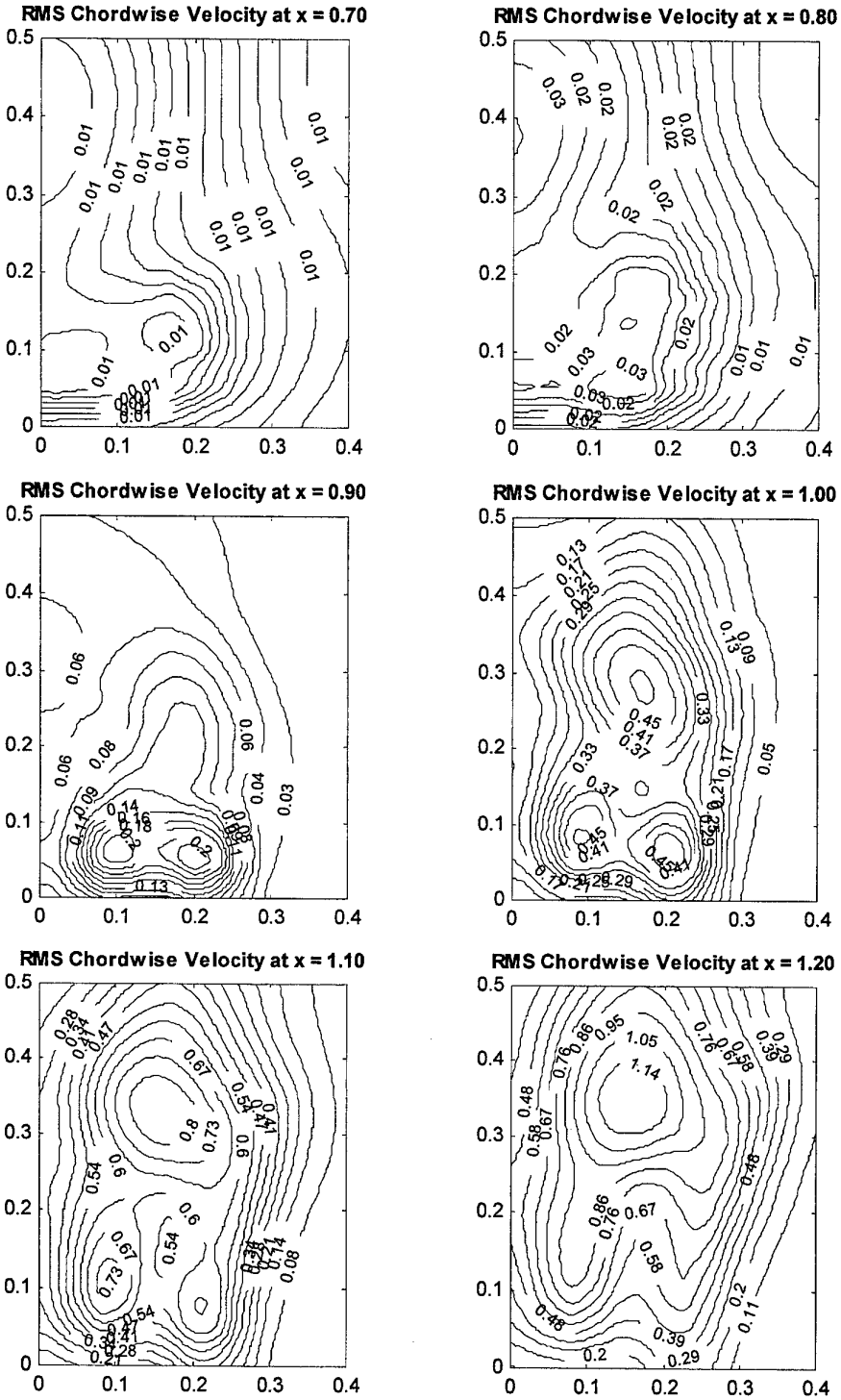

Figure 12 Distribution of RMS chordwise velocities at 30 degrees angle of attack.

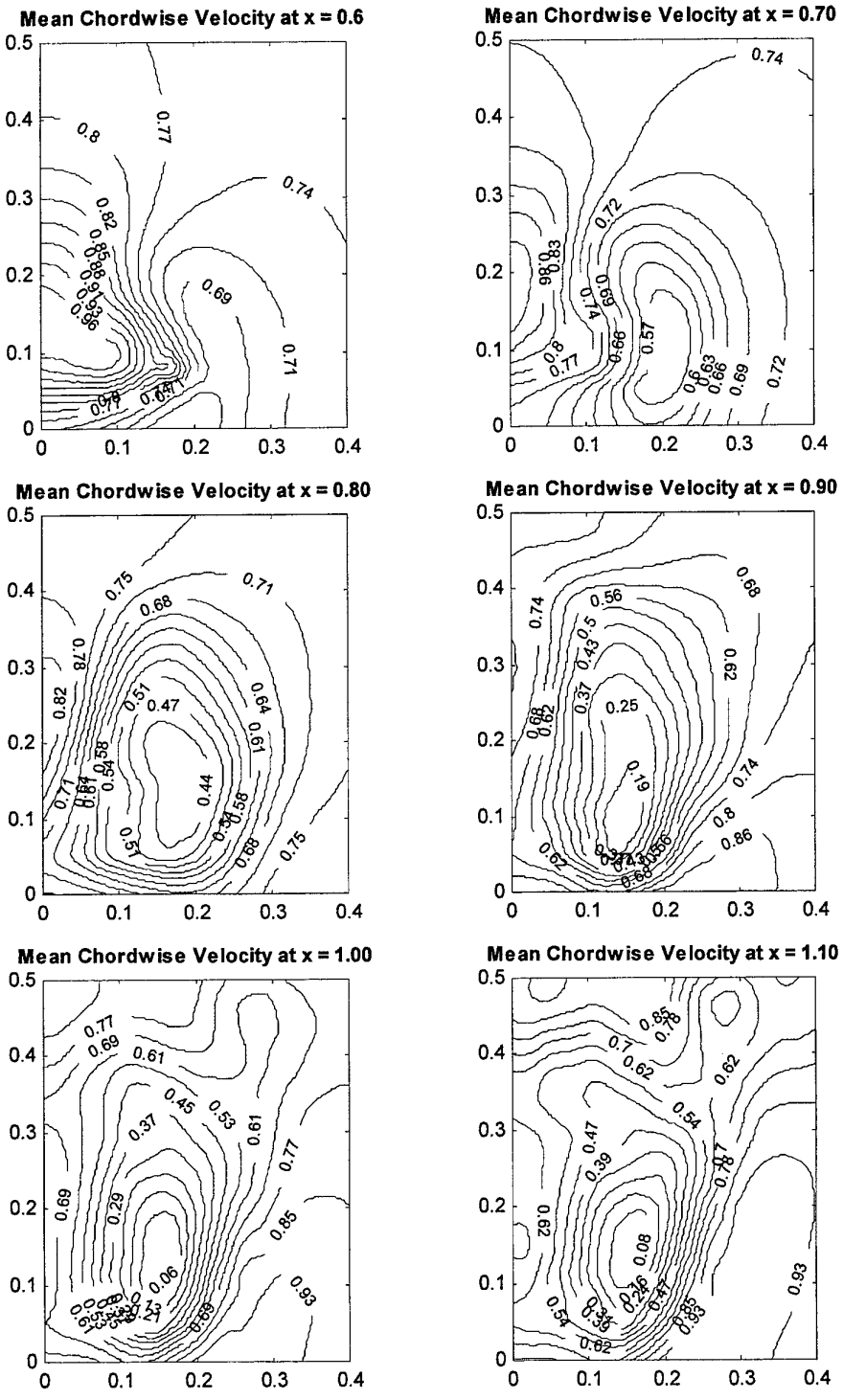

Figure 13 Distribution of mean chordwise velocities at 40 degrees angle of attack.

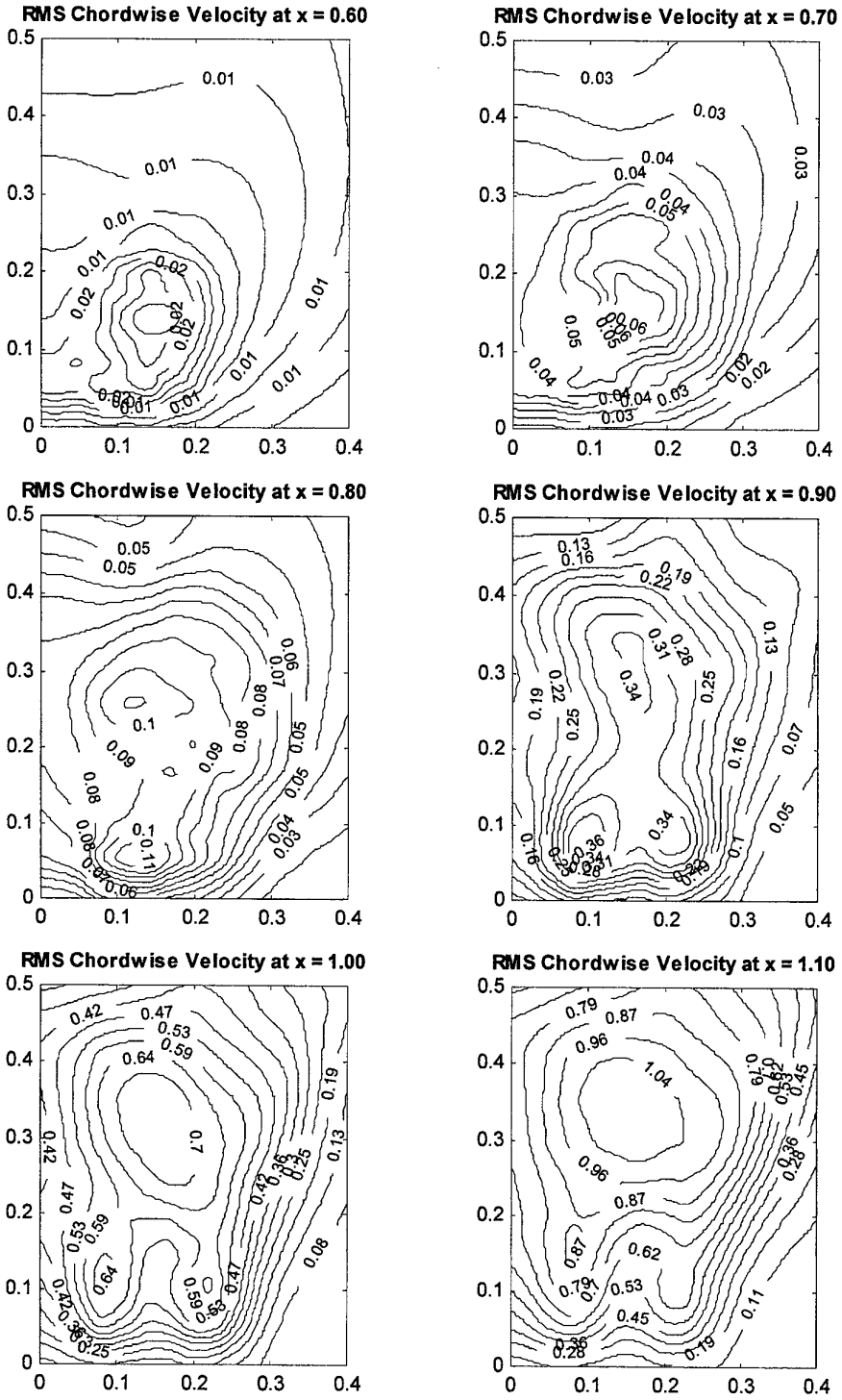

Figure 14 Distribution of RMS chordwise velocities at 40 degrees angle of attack.

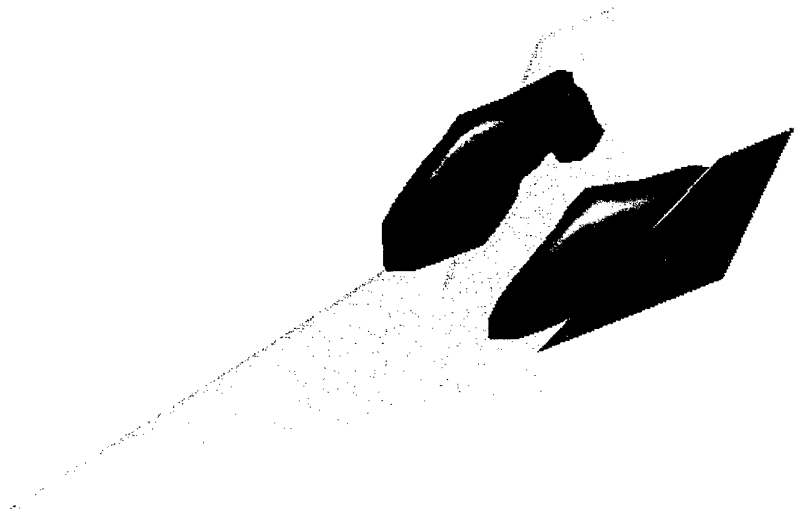

Figure 15 Iso-surfaces of time-averaged pressure coefficient of 0.88 at 30 degrees angle of attack.

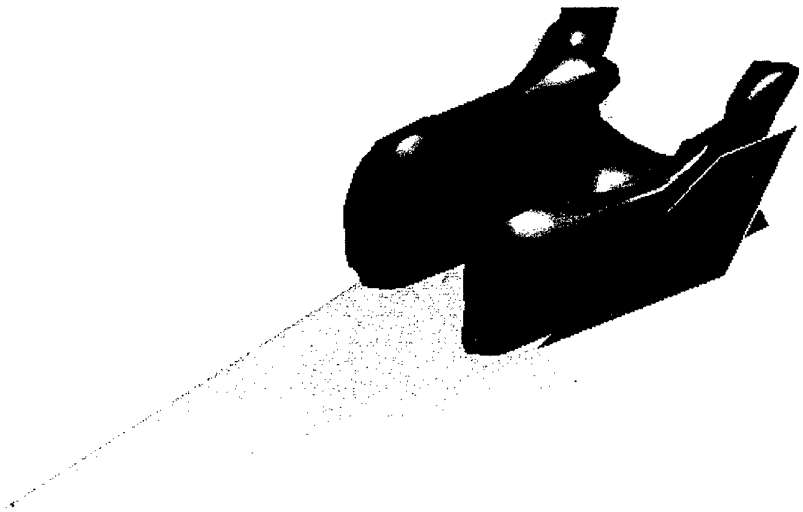

Figure 16 Iso-surfaces of time-averaged pressure coefficient of 0.88 at 40 degrees angle of attack

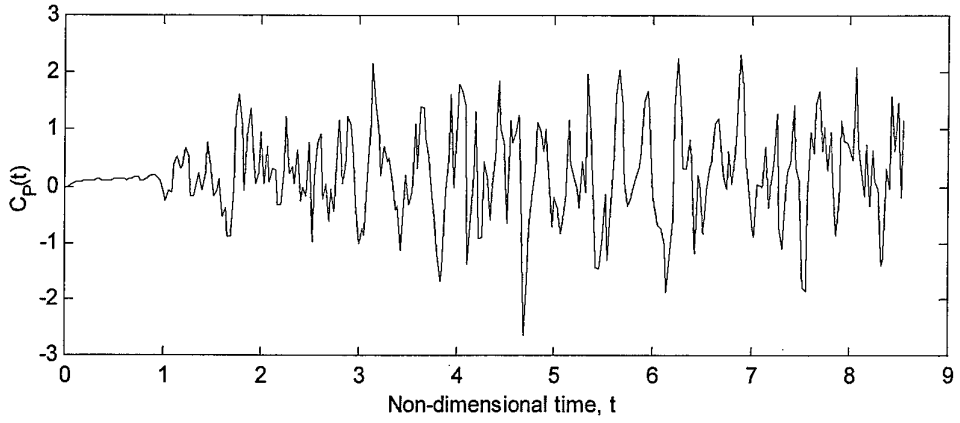

Figure 17 Time history of differential pressure at 45% chord and 60% span location on fin at 30-degrees angle of attack.

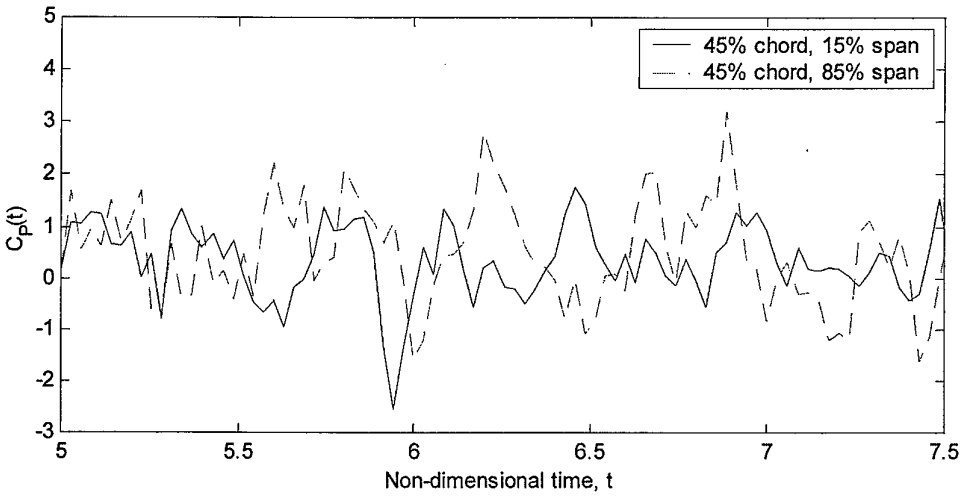

Figure 18 Time history of differential pressure at root and tip locations on fin at 30-degrees angle of attack

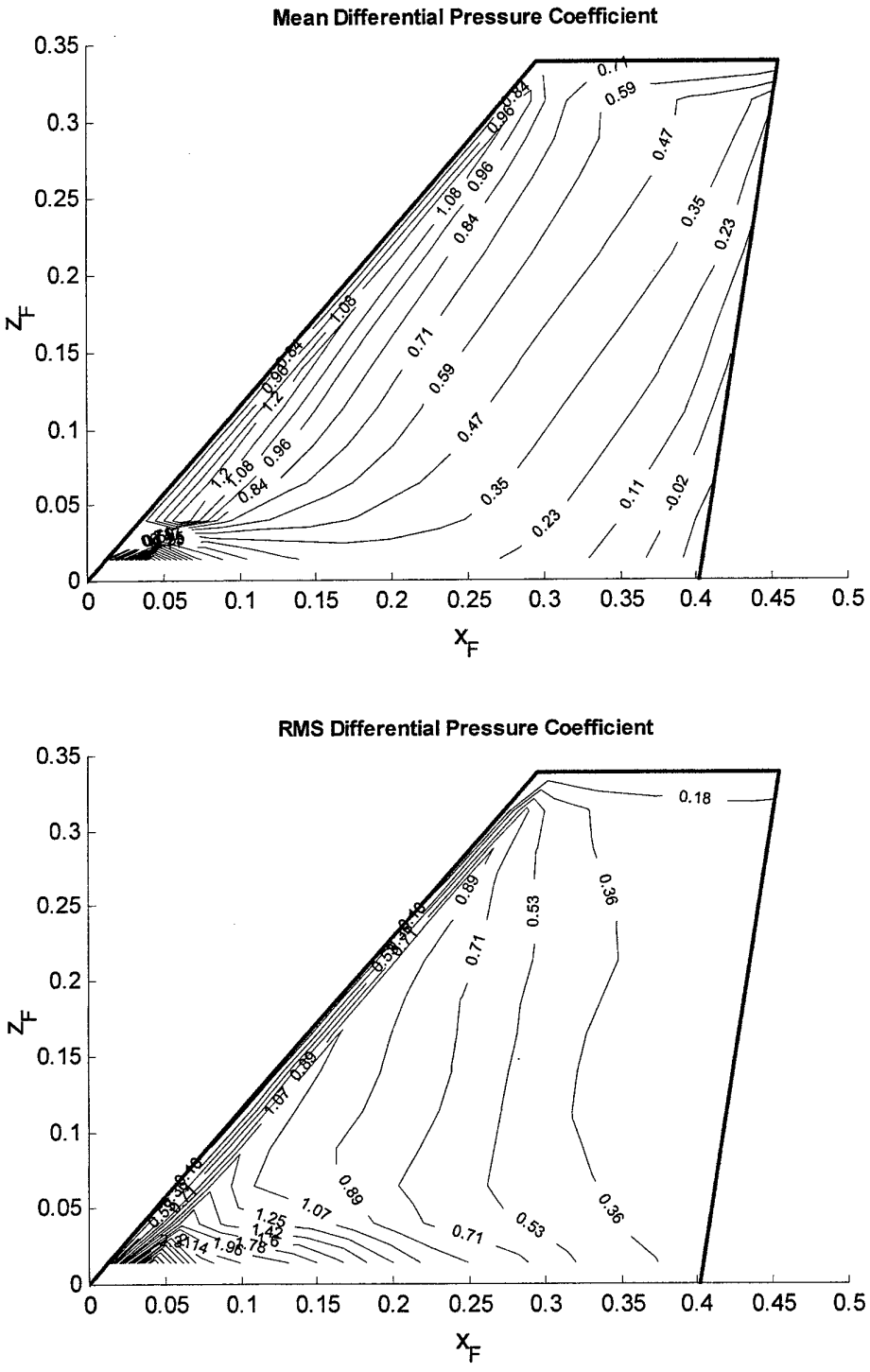

Figure 19 Distribution of differential pressure over the fin at 20 degrees angle of attack

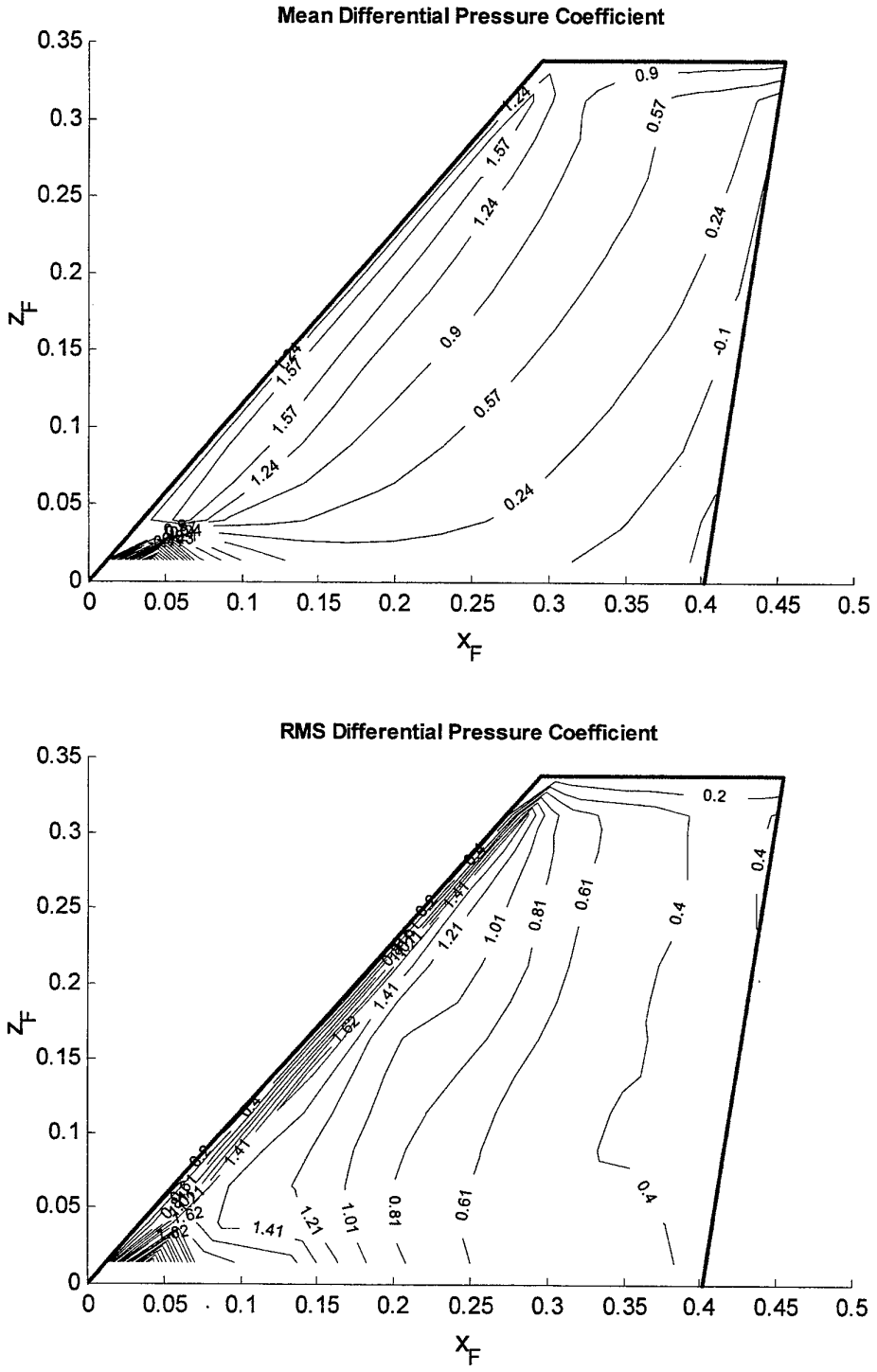

Figure 20 Distribution of differential pressure over the fin at 30 degrees angle of attack

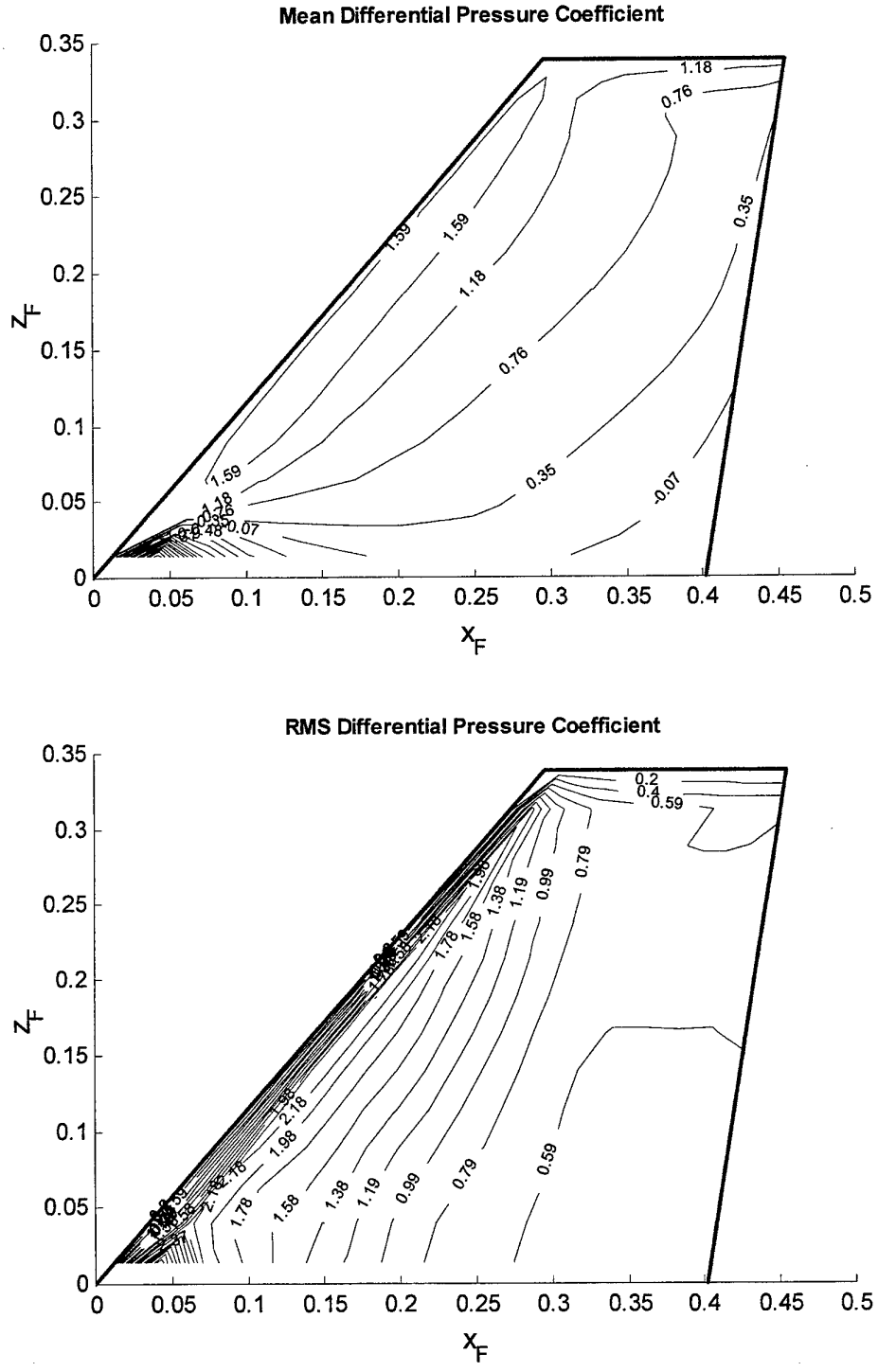

Figure 21 Distribution of differential pressure over the fin at 40 degrees angle of attack

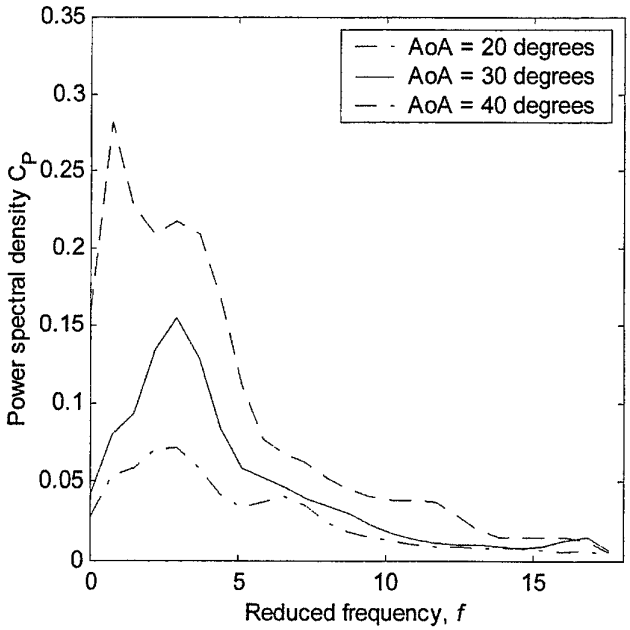

Figure 22 Variation of power spectral density of differential pressure with angle of attack

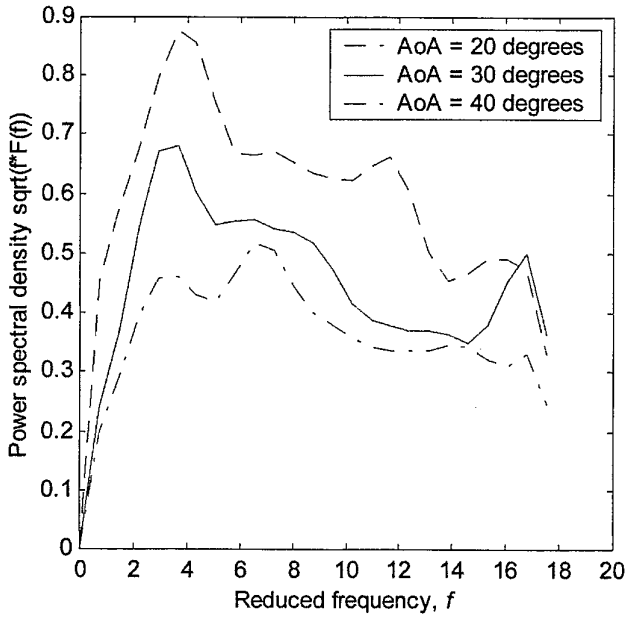

Figure 23 Variation of buffet excitation spectra with angle of attack

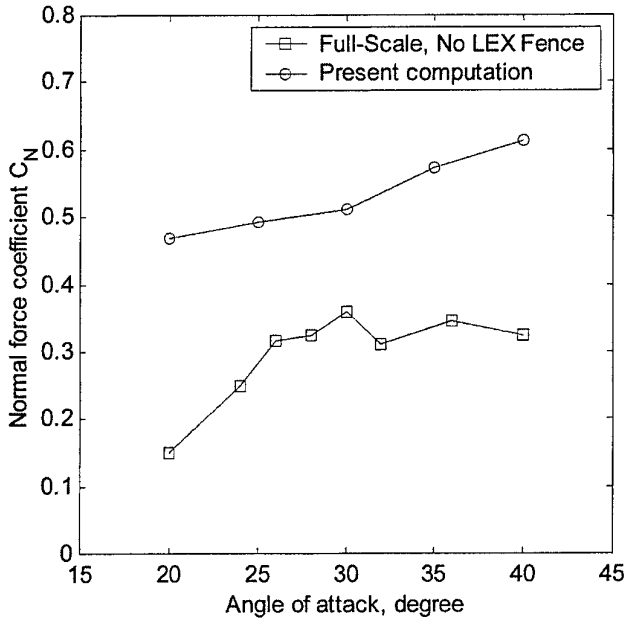

Figure 24 Comparison of mean normal force coefficient

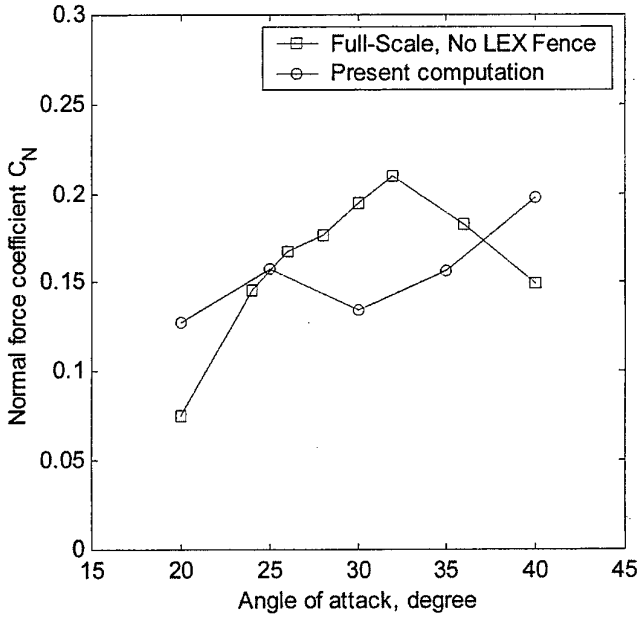

Figure 25 Comparison of RMS normal force coefficient

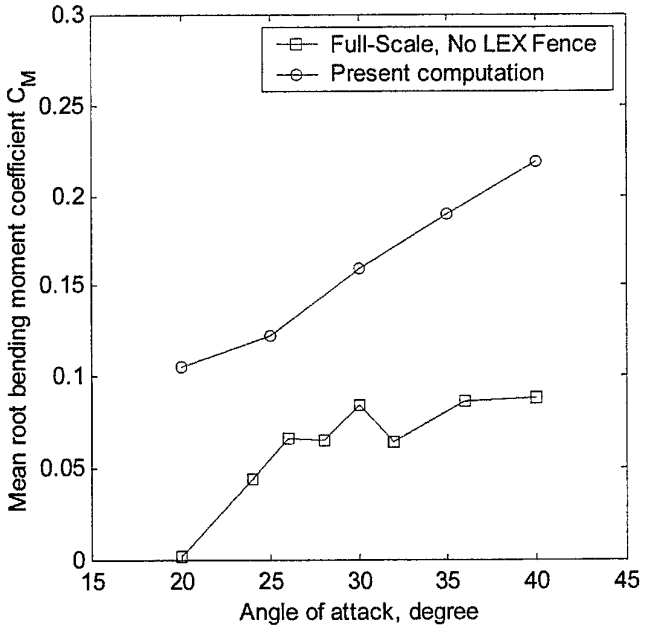

Figure 26 Comparison of mean tail root bending moment coefficient

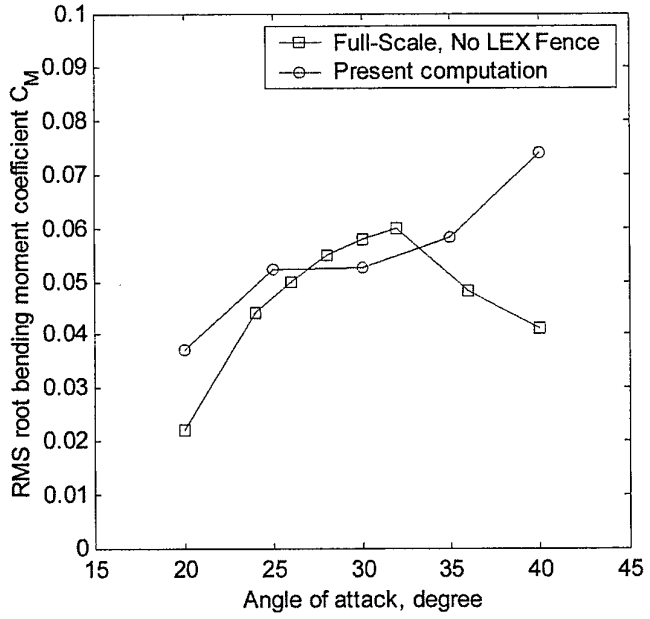

Figure 27 Comparison of RMS tail root bending moment coefficient

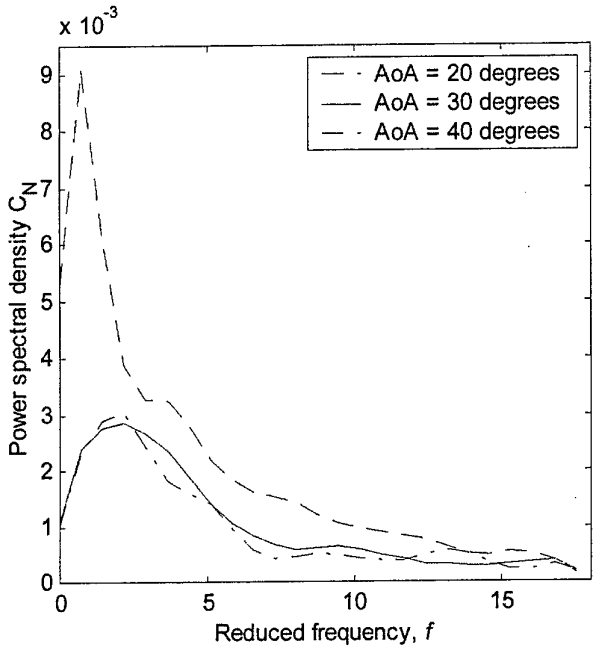

Figure 28 Variation of normal force power spectral density with angle of attack

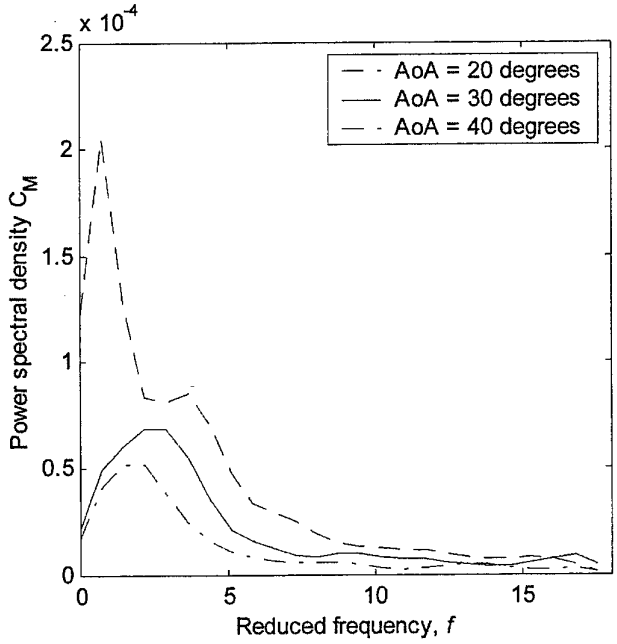

Figure 29 Variation of bending moment power spectral density with angle of attack

DISTRIBUTION LIST

Prediction of Buffet Loads on Twin Vertical Tails Using a Vortex Method

Oleg Levinski

AUSTRALIA

DEFENCE ORGANISATION

Task Sponsor	**CDR ARDU**	1

S&T Program

Chief Defence Scientist	shared copy
FAS Science Policy	
AS Science Corporate Management	
Director General Science Policy Development	
Counsellor Defence Science, London	(Doc Data Sheet)
Counsellor Defence Science, Washington	(Doc Data Sheet)
Scientific Adviser to MRDC Thailand	(Doc Data Sheet)
Scientific Adviser Joint	1
Navy Scientific Adviser	(Doc Data Sheet and distribution list)
Scientific Adviser - Army	(Doc Data Sheet and distribution list)
Air Force Scientific Adviser	1
Director Trials	1

Aeronautical and Maritime Research Laboratory

Director	1
Chief of Airframes and Engines Division	1
Research Leader Structural Integrity	1
Task Manager (Peter Farrell)	1
Author: Dr. Oleg Levinski	2
Loris Molent	1
David Conser	1

DSTO Library and Archives

Library Fishermans Bend	(Doc Data sheet)
Library Maribyrnong	(Doc Data sheet)
Library Salisbury	1
Australian Archives	1
Library, MOD, Pyrmont	(Doc Data sheet)
US Defense Technical Information Center	2
UK Defence Research Information Centre	2
Canada Defence Scientific Information Service	1
NZ Defence Information Centre	1
National Library of Australia	1

Capability Systems Staff

Director General Maritime Development	(Doc Data Sheet only)
Director General Aerospace Development	1

Knowledge Staff

Director General Command, Control, Communications and Computers (DGC4) (Doc Data Sheet only)

Director General Intelligence, Surveillance, Reconnaissance, and Electronic Warfare (DGISREW)R1-3-A142 CANBERRA ACT 2600 (Doc Data Sheet only)

Director General Defence Knowledge Improvement Team (DGDKNIT) R1-3-A141, CANBERRA ACT 2600 (Doc Data Sheet only)

Army

ABCA Standardisation Officer, Puckapunyal	4
SO (Science), DJFHQ(L), MILPO Enoggera, Queensland 4051	(Doc Data Sheet)
NAPOC QWG Engineer NBCD c/- DENGRS-A, HQ Engineer Centre Liverpool Military Area, NSW 2174	(Doc Data Sheet)

Air Force

Aircraft Research and Development Unit	1
DGTA	1

Intelligence Program

DGSTA Defence Intelligence Organisation	1
Information Centre, Defence Intelligence Organisation	1

Corporate Support Program

Manager DLS- Canberra	1

UNIVERSITIES AND COLLEGES

Australian Defence Force Academy	1
Library	1
Head of Aerospace and Mechanical Engineering	1
Serials Section (M list), Deakin University Library, Geelong	1
Senior Librarian, Hargrave Library, Monash University	(Doc Data Sheet)
Librarian, Flinders University	1

OTHER ORGANISATIONS

NASA (Canberra)	1
AusInfo	1

OUTSIDE AUSTRALIA

ABSTRACTING AND INFORMATION ORGANISATIONS

Library, Chemical Abstracts Reference Service	1
Engineering Societies Library, US	1
Materials Information, Cambridge Scientific Abstracts, US	1
Documents Librarian, The Center for Research Libraries, US	1

INFORMATION EXCHANGE AGREEMENT PARTNERS

Acquisitions Unit, Science Reference and Information Service, UK	1
Library - Exchange Desk, National Institute of Standards and Technology, US	1
National Aerospace Laboratory, Japan	1
National Aerospace Laboratory, Netherlands	1
SPARES	5
Total number of copies:	**52**

DEFENCE SCIENCE AND TECHNOLOGY ORGANISATION
DOCUMENT CONTROL DATA

1. PRIVACY MARKING/CAVEAT (OF DOCUMENT)

2. TITLE

Prediction of Buffet Loads on Twin Vertical Tails Using a Vortex Method

3. SECURITY CLASSIFICATION (FOR UNCLASSIFIED REPORTS THAT ARE LIMITED RELEASE USE (L) NEXT TO DOCUMENT CLASSIFICATION)

Document	(U)
Title	(U)
Abstract	(U)

4. AUTHOR(S)

Oleg Levinski

5. CORPORATE AUTHOR

Aeronautical and Maritime Research Laboratory
506 Lorimer St
Fishermans Bend, Victoria 3207 Australia

6a. DSTO NUMBER	6b. AR NUMBER	6c. TYPE OF REPORT	7. DOCUMENT DATE
DSTO-RR-0217	AR-011-966	Research Report	July, 2001

8. FILE NUMBER	9. TASK NUMBER	10. TASK SPONSOR	11. NO. OF PAGES	12. NO. OF REFERENCES
M1/9/890	AIR 00/142	CDR ARDU	69	39

13. URL on the World Wide Web

http://www.dsto.defence.gov.au/corporate/reports/DSTO-RR-0217.pdf

14. RELEASE AUTHORITY

Chief, Airframes and Engines Division

15. SECONDARY RELEASE STATEMENT OF THIS DOCUMENT

Approved for public release

OVERSEAS ENQUIRIES OUTSIDE STATED LIMITATIONS SHOULD BE REFERRED THROUGH DOCUMENT EXCHANGE, PO BOX 1500, SALISBURY, SA 5108

16. DELIBERATE ANNOUNCEMENT

No Limitations

17. CASUAL ANNOUNCEMENT Yes

18. DEFTEST DESCRIPTORS

F/A-18 aircraft, Aft fuselages, Tail assemblies, Fatigue tests, Buffeting, Aerodynamics, Unsteady flow, Vortices, Vortex flow, International FollowOn Structural Test Project

19. ABSTRACT

The work is concerned with the computation of F/A-18 vertical tail buffet due to LEX vortex burst using vortex methods of unsteady flow modelling. It is recognised that prediction of buffet loading requires accurate modelling of the unsteady pressure field past a burst LEX vortex. To reduce computational overheads associated with simulation of flow over the complete aircraft, a more generic delta-wing, twin vertical-tail configuration was used for initial studies. The aim is to generate an unsteady, vortex-breakdown flow using a delta wing and to place a vertical tail, which is cantilevered, downstream of the vortex breakdown flow. The paper describes the development of an unsteady vortex model for prediction of buffet loads and its validation against experimental data. Results of computation indicate that the vortex model is able to predict the onset of leading edge vortex breakdown and qualitatively describe the characteristics of unsteady buffet pressures arising on the rigid tail.